Mixing at the Ocean's Bottom Boundary

Kurt L. Polzin[1][*][†] and Trevor J. McDougall[2][†]

[1]Department of Physical Oceanography, Woods Hole Oceanographic Institution,
Woods Hole MA 02543, USA

[2]School of Mathematics and Statistics, University of New South Wales, Sydney,
NSW 2052, Australia

[*]Corresponding author. Email: kpolzin@whoi.edu

[†]These authors contributed equally to this work.

Abstract

The lower limb of the global overturning circulation represents the transformation of waters previously made dense by cryogenic processes around Antarctica that have found their way to the oceans' bottom. Along the pathways north, these waters are made warmer and lighter. The essential character of the lower limb is defined by the importance of upwelling across density surfaces (isopycnals) rather than pathways that are largely along isopycnals. This crossing of isopycnals is accomplished via turbulent mixing and our current understanding is that the turbulent transformations predominantly occur near the ocean's bottom boundary. The intent of this chapter is to review the intellectual foundations underpinning the lower limb and to summarize the observational grounding. Both the theory and observations of the upwelling in the abyss are in the early stages of changing paradigms, and the efforts here to connect the two approaches are unsatisfying. Reconciling deep-ocean mixing observations and theories is unfinished business, and should remain an exciting field for another generation of oceanographers.

key words: ocean mixing, diapycnal mixing, upwelling, downwelling, bottom water, abyssal mixing

1   Introduction

Once upon a time, at the dawn of modern oceanography, there was a great influx of money and the creation of many near continuously measuring instruments. These included instruments like the Neil Brown Mark III CTD (Brown, 1974) which permitted < 1 meter resolution of temperature, salinity and pressure; Sanford's Electro-Magnetic Velocity Profiler (Sanford, 1975), which provided, for the first time, direct observations of oceanic horizontal velocity at ten meter vertical resolution; long term moored observations of horizontal currents and temperature that led to a quantitative understanding of the spatial distribution of mean flows and eddy variability (via the Mid-Ocean

Dynamics Experiment (MODE, Group et al. (1978); PolyMODE, Kamenkovich et al. (1986); etc.). These new observations opened a multitude of avenues to explore the question, "How does water rise from the abyss to the bottom of the thermocline?" posed, for example, by Munk (1966), but this was by no means the origin of that question (e.g. Wyrtki, 1961, 1962).

This takes us to what we call Armi v. Garrett, after their 1979 exchange (Armi, 1979b; Garrett, 1979). Armi and Millard Jr (1976) and Armi (1978) were attempting to interpret steps in abyssal temperature and salinity traces returned by the new fangled Neil Brown instrument as detached mixed layers and linking those to the issue of complex topography, figure 1. Garrett, on the other hand, promotes a seductive figure of a well mixed boundary layer over a planar sloping bottom, figure 2. The crux of this 'conversation' can be posed as a question: 'at what rate are you mixing in boundary layers that are well mixed?' with the backdrop of, 'how important are boundary processes relative to interior mixing associated with an intermittent internal wave breaking process in the interior?' Our understanding has grown significantly since that exchange. With four decades worth of perspective, Armi was likely speaking to mixing as the end product of dynamical processes, indirectly coupled to a frictional bottom stress, and an actual theoretical paradigm has been created for the figure sketched by Garrett. The reason for *this* preamble is that the dichotomy in that exchange not only is still in play today, it structures this review. The core issue is that, however reasonable a representation of the bottom boundary layer figure 2 might seem to be, when you start to look at the ocean, one finds great sympathy for figure 1.
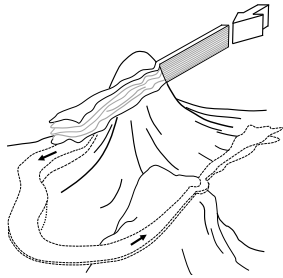

Figure 1: A schematic characterization of flow-topography interaction, boundary layer production and flow separation. Note, amongst other things, that the ocean's bottom is not depicted as a planar sloping boundary. Figure redrawn from Armi (1979a).
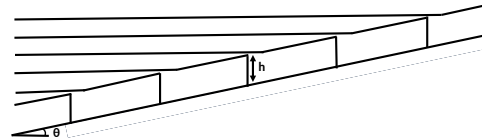
Figure 2: A schematic representation of the bottom boundary layer over a planar sloping boundary. Figure redrawn from Garrett (1979). This schematic is a prototype for more sophisticated discussions below.

Munk (1966) suggests several avenues by which the global upwelling of deep waters might be accomplished. One of these is that of mixing resulting from interactions between internal waves, akin to how one might consider white capping in a surface wavefield to be the end process of interactions between surface waves, for which the theoretical underpinnings (Phillips, 1960; Hasselmann, 1962) were just beginning to be articulated. With this option one might argue internal wave breaking and mixing to be broadly distributed in space. This path takes us past the articulation of a two-dimensional internal wave spectrum (Garrett and Munk, 1972b) from which the space-time

variations of mixing events can be estimated (Garrett and Munk, 1972a) and concerted efforts to provide a theoretical paradigm for nonlinear interactions between internal waves (Olbers, 1976; McComas and Bretherton, 1977; Pomphrey et al., 1980). Coupled with a growing ability to measure oceanic turbulence using specialized sensors (Nasmyth, 1970; Gregg and Cox, 1971; Osborn and Siddon, 1973), theory, kinematic mixing models employing finestructure observations and direct turbulence measurements provided an evolving appreciation (Garrett, 1984) that the background internal wavefield supports a diffusivity of $1 \times 10^{-6} - 1 \times 10^{-5}$ m^2 s^{-1} in the main thermocline, an order of magnitude smaller than Munk's abyssal mixing metric of $K_\rho = 1 \times 10^{-4}$ m^2 s^{-1} required to permit the net upwelling of some 30×10^6 m^3 s^{-1}. A second avenue mentioned in Munk (1966) consists simply of a suggestion of strong mixing along the ocean boundaries due to current shear and internal wave breaking being efficiently communicated into the interior along isopycnal surfaces (Schiff, 1966). This is the paradigm that underpins Armi vs. Garrett. The viability of this boundary mixing scenario was increasingly underscored by simple heat budgets (made possible by long term deployments of current meter arrays (Hogg et al., 1982; Whitehead Jr and Worthington, 1982) for abyssal basins that implied the deep ocean hosted significantly larger diapycnal diffusivities.

The box on this problem was fully opened in the context of a large multi-national field program that produced a control volume for dense water entering and exiting the deep Brazil Basin (Morris et al., 2001). Many of the key issues are manifested in the iconic section of diapycnal diffusivity (K_ρ) estimates from the Brazil Basin Tracer Release Experiment, figure 3. Over the western side of the Brazil Basin, turbulent mixing is small ($K_\rho < 1 \times 10^{-5}$ m^2 s^{-1}) and nearly independent of depth. On the eastern side of the basin, K_ρ is an order of magnitude larger at mid-depth and increases by another order of magnitude as the bottom is approached. The key to this pattern lies in the bottom topography: On the western boundary the bottom is weakly sloping. In the east, over the Mid-Atlantic Ridge, the bottom topography is steep and rough. Associated with the pattern of increasing turbulent diffusivity with depth is an increase in turbulent dissipation which, if taken at face value, implies downwelling.[1] This inference of downwelling contradicts the net watermass budgets for the deep Brazil Basin, in which more dense water enters than leaves, demanding net upwelling across isopycnals.

The focus of this review is the maintenance of the deep overturning cell: the processes and mechanisms which support the 3-D turbulence responsible for the flow across dense isopycnals and the representation of such processes in general circulation models (GCMs). There are closely allied questions of tracer dispersion and watermass transformation, horizontal circulations related to the mixing distributions and transport of mixed water from the boundary that we touch upon. We start this review by covering the things we can agree on in Section 2. These are equations and the importance of non-dimensional parameters in organizing our thoughts. Section 3 reviews idealized modeling and GCM behavior. Section 4 then tends to issues of observational inference directed to elucidating the idealized nature of the preceding section. After summarizing in section 5 we will attempt to describe pathways to answer open questions. We are aided by substantial reviews

---

[1]Not that this is obvious. If turbulent intensity varies in space, a tracer's center of mass will be drawn in the direction of more intense turbulence. See section 2.3 for discussions about the flows across density surfaces driven by variations in turbulent intensity.
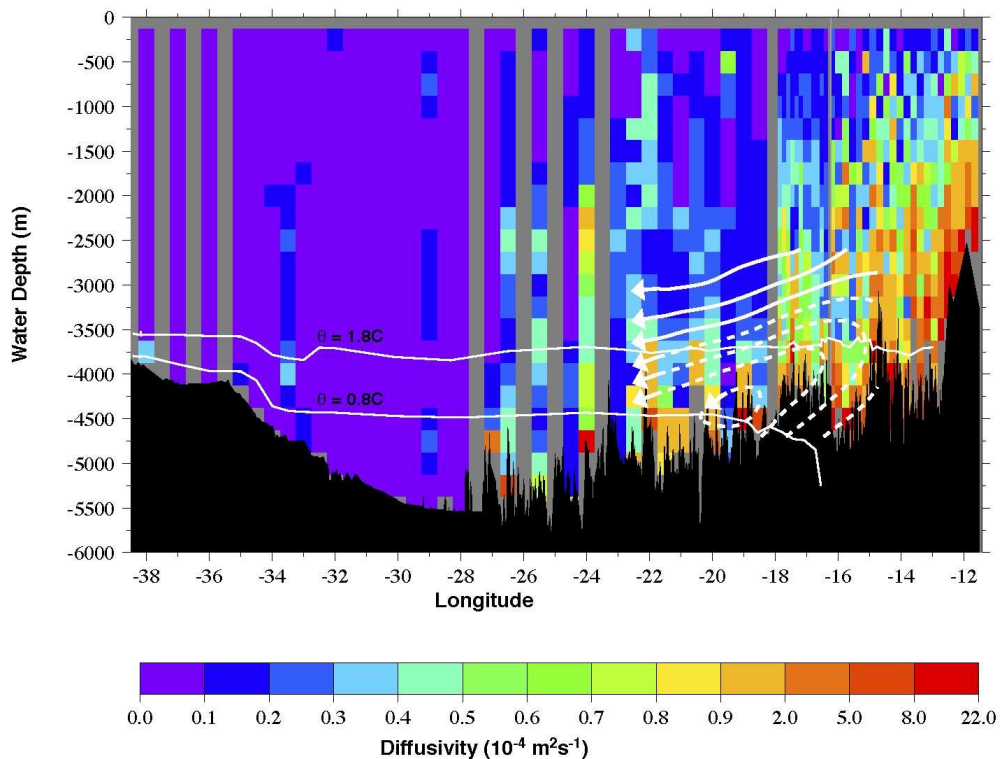
Figure 3: Depth-longitude section of diapycnal diffusivity K_ρ in the Brazil Basin. The figure appears in Mauritzen et al. (2002), with data originally reported in Polzin et al. (1997) and Ledwell et al. (2000). Note the nonuniform color map. The thin white lines mark the observed depth of the 0.8 and 1.8 C potential isotherms. The thicker white lines with arrows are a schematic representation of the stream function estimated from an inverse calculation (St. Laurent et al., 2001) and are intended to portray the zonal overturning circulation and modification of Bottom Water in the Brazil Basin.

concerning the forcing of turbulence by topographic internal gravity waves (Sarkar and Scotti, 2017), the details of buoyancy fluxes in relation to turbulent kinetic energy production and dissipation in stratified flows (Gregg et al., 2018) and bottom boundary layer physics (Trowbridge and Lentz, 2018) that gratefully limit our discussion.

2   Common Ground

The plot line for writing a story about global ocean upwelling is deceptively simple. In steady state, the velocity across an isopycnal is proportional to the divergence of the turbulent density flux and one wants the net transformation to be equal to the rate at which dense water is formed. With boundary mixing, though, the plot line immediately branches because we need to consider both the magnitude of that turbulent buoyancy flux and the relevant spatial scales. In this section we gather

together seemingly disparate threads to create a common language for a discussion about "boundary mixing" and elucidate ambiguities of interpretation that have arisen.

2.1   Equations

We start from a Reynolds decomposition of the equations of motion, in which variables ϕ have been decomposed into a mean $\overline{\phi}$ and perturbation ϕ'. This act itself carries with it a certain ambiguity: The mean could represent time invariant conditions or slowly varying subinertial times scales, or even internal waveband processes. The perturbation could represent subinertial times scales, internal waves (superinertial) or 2-dimensional and or 3-dimensional turbulence. In section 4 we discuss a variety of phenomena which imply the locus of turbulent fluxes is within the internal waveband over steep and rough topography. In the following, the three-dimensional velocity is $\mathbf{u} = (u, v, w)$, ρ is density, g is gravity, f is the Coriolis parameter relating to the local pendulum day and p is pressure. A bold font is used to indicate a vector quantity. The Reynolds averaged equations are

$$\frac{\partial \overline{u}}{\partial t} + \overline{\mathbf{u}} \cdot \nabla \overline{u} + \nabla \cdot \overline{u'\mathbf{u}'} - f\overline{v} \;=\; -\frac{1}{\rho_0}\frac{\partial \overline{p}}{\partial x} \tag{1a}$$

$$\frac{\partial \overline{v}}{\partial t} + \overline{\mathbf{u}} \cdot \nabla \overline{v} + \nabla \cdot \overline{v'\mathbf{u}'} + f\overline{u} \;=\; -\frac{1}{\rho_0}\frac{\partial \overline{p}}{\partial y} \tag{1b}$$

$$\frac{\partial \overline{w}}{\partial t} + \overline{\mathbf{u}} \cdot \nabla \overline{w} + \nabla \cdot \overline{w'\mathbf{u}'} \;=\; -\frac{1}{\rho_0}\frac{\partial \overline{p}}{\partial z} - \overline{b} \tag{1c}$$

$$\frac{\partial \overline{\rho}}{\partial t} + \overline{\mathbf{u}} \cdot \nabla \overline{\rho} + \nabla \cdot \overline{\rho'\mathbf{u}'} \;=\; 0 \tag{1d}$$

in which variations of density in the momentum equations are retained only when they appear in terms multiplied by gravity g; buoyancy is $b = -g(\rho - \rho_0)/\rho_0$; and ρ_0 is a constant reference density. Equations (1) are complemented by a continuity equation, $\nabla \cdot \mathbf{u} = 0$. The direct impacts of molecular processes are assumed to be small with respect to the effects of turbulent transports: there is an inner scale of turbulent microstructure where gradient variances are dissipated by molecular processes. This scale is much smaller than the 'outer' scales that characterize the turbulent fluxes.

A common device is to describe the net effects of turbulent fluxes $\mathbf{F}_\phi$ using flux-gradient relations, which in turn has an intellectual grounding in mixing length theory. In one dimension:

$$F_\phi \equiv \overline{u'_\perp \phi'} = -K_\phi \nabla_\perp \overline{\phi} \qquad \text{flux} - \text{gradient relation} \tag{2a}$$

$$\phi' = \ell_{\mathrm{mix}} \nabla_\perp \overline{\phi} \qquad\qquad \text{mixing length} \tag{2b}$$

in which $u'_\perp$ is normal to mean isopleths of $\overline{\phi}$, $\nabla_\perp \overline{\phi}$ is the normal gradient and ℓ_{mix} the 'mixing length'. This comes with important caveats: it is a 'local' closure relating K_ϕ to the gradient at that point. As such it is unlikely to be an accurate summary of convection set up in a downwelling Ekman layer (section 4.3) or near boundary wave overturning relating to linear internal wave kinematics (section 4.1) rather than dynamical instabilities, or situations in which turbulent transport terms contribute to a scalar variance budget (section 2.5.2).[2]

---

[2]This flux-gradient relation is applicable only to variables that possess the "potential" property whereby the

A further equation describes the evolution of a passive tracer, whose concentration we will denote by C:[3]

$$\frac{\partial \overline{C}}{\partial t} + \overline{\mathbf{u}} \cdot \nabla \overline{C} + \nabla \cdot \overline{C' \mathbf{u'}} = 0 \tag{3}$$

2.2   Boundary Conditions

One of the more bedeviling issues with boundary mixing is that there is not simply one process or one relevant boundary layer height scale. Rather, there is a hierarchy as one considers larger and longer space-time scales and the dynamical balances that dictate the boundary layer structure change. While molecular viscosity acts to bring the velocity at the boundary to zero, i.e. $\mathbf{u}(x, y, z = h) = 0$, this happens within a viscous sublayer on scales smaller than one centimeter embedded within a log-layer, in which the only dynamically relevant length scale is the distance from the boundary, (e.g. Tennekes and Lumley, 1972). In the far-field of this log-layer, in excess of 1000 times wall unit lengths of ν/u_* with molecular viscosity ν and 'friction velocity' $u_* = \sqrt{\tau/\rho}$ dependent upon the bottom stress τ, one has a situation in which the velocity profile joins the 'free-stream'. The object of turbulence modelling with full blown closure schemes (e.g. Weatherly and Martin, 1978; Taylor and Sarkar, 2008) is to estimate the evolution of turbulent kinetic energy and turbulent length scales as a function of height above bottom, from which the momentum and buoyancy fluxes, and thus eddy viscosity/diffusivity (2) follow. This turbulence modelling paradigm permits, in particular, the *prediction* of eddy viscosity / diffusivity profiles in response to stratification, rotation, or pressure gradients as a function of height above bottom.

The theoretical work discussed here is of different intent. In this work one generally *assumes* vertical profiles of eddy diffusivity and, from a constant ratio of eddy viscosity A to eddy diffusivity K (i.e. a Prandtl number), solves for the structure of the boundary layer; and then relates that structure to global ocean behavior. This requires some fortitude. From the perspective of the planetary boundary layer, 1000 wall units is quite small. At a free stream velocity of 0.20 m s^{-1}, 1000 wall units is less than 0.2 meters. There are two things to keep in mind. First, this theoretical work will use a no flow condition on the velocity at the boundary without attempting a self consistent structure in the vertical for the turbulent dynamics. There is a rich history in this problem of *ad hoc* assumptions about the spatial structure of eddy diffusivity and viscosity which, in combination with no-flux and no-flow boundary conditions provide a mathematically well posed problem from which analytic or simple numerical solutions can provide significant insight. We report on these in considerable detail in section 3. There are issues, though. These assumed profiles, Prandtl numbers and boundary conditions do not correspond to the output of any realistic turbulence closure scheme. We try to cover some of this ground in section 4.3. Second, there are precious few near bottom observations that serve as constraints. With this intent, the boundary conditions for the Reynolds averaged equations (1) are:

---

variable is unchanged by adiabatic and isohaline changes in pressure. Examples of variables that are not "potential" variables are in situ temperature, in situ density, specific volume anomaly, and enthalpy (IOC, 2010).

[3]This conservative form of an evolution equation for a variable is only applicable to variables that possess the "conservative" property whereby the total amount of the property remains the same when two parcels are brought together and mixed to completion. Examples of variables that are not "conservative" variables are potential temperature, potential density and entropy (IOC, 2010).

$$\mathbf{u}(z = h) = 0 \quad vis \quad \overline{u'u'_{\perp}} = \frac{1}{2}C_d\overline{\mathbf{u}}\,|\overline{u}| \tag{4a}$$

$$\mathbf{u}\cdot\nabla h(x,y) = 0 \tag{4b}$$

$$\nabla_{\perp}C(z = h) = 0 \quad vis \quad \overline{\mathbf{u}'C'}\cdot\nabla h = 0 \tag{4c}$$

The first equation (4a) represents both the molecular condition of no flow at the bottom (where $z = h(x,y)$) and a quadratic drag formulation for the bottom normal stress, nominally $C_d = 2-3\times10^{-3}$. The quadratic drag formulation assumes that the afore-mentioned hierarchy of boundary layers is turbulent, which is generally, but not always the case (Ruan et al., 2019; Kaiser and Pratt, 2020), to be employed when one is not resolving the log layer. The bottom normal velocity is represented as $\overline{u}_{\perp}$ and h represents the equation of the boundary. The second (4b) is a statement that the bottom is a material surface and that fluid parcels on that surface remain there. The third (4c) represents both the molecular condition of no-flux, in which $\nabla_{\perp}C$ is the boundary normal gradient, and a statement that the turbulent flux of a quantity C normal to the boundary is zero.

Subtly hidden within the kinematic statement of no flow through the boundary (4b) is that the pressure field arranges itself to accommodate (4b) and thereby represents a potential drag. This can be more clearly seen by integrating the Reynolds averaged equations (1) in the vertical and using Leibniz's integration rule:

$$\int_{h(x,y)}^{z_0} dz\nabla_{x,y}p(x,y,z) = \nabla_{x,y}\int_{h(x,y)}^{z_0} dz\ p(x,y,z) + p(x,y,z = h(x,y))\nabla_{x,y}h(x,y) \tag{5}$$

in which $\nabla_{x,y}$ is the horizontal gradient operator and z_0 represents a reference height. The correlation of pressure with height gradients along the bottom boundary ($p\nabla h$) is termed 'form drag'. Form drag represents the conversion of energy between mean and perturbation fields, (with total energy conservation following from $p\mathbf{u}\cdot\nabla h = 0$), placing energy into the perturbation fields where it is more prone to mixing.

Both form drag (5) and bottom drag (4a) represent sources for turbulent mixing and can be of comparable size for finite amplitude topography, section 4.2. There is an essential difference, though. The stress driven turbulence acts on scales of 10-s of meters while form drag acts over height scales of 100-s of meters in the abyssal ocean, section 4.2.

2.3   Coordinate Transformations and the One Dimensional Model

The equations of motion are cast in a Cartesian (x, y, z) coordinate system. While this emphasizes the fact that gravity defines the vertical coordinate and Earth's rotation impacts the horizontal velocities, distinctions which are fundamental in geophysical fluid dynamics, significant simplification and intuition can be attained via analytic solutions to a one-dimensional representation by representing the bottom as an infinite sloping plane, figure 4

$$z = -h_0 + \alpha x\ .$$

with h_0 being an arbitrary constant and $\alpha = \tan(\theta)$ is the topographic slope.

Rotation to a Semi-Infinite Plane

Here one assumes the mean can be further decomposed into $\overline{\phi} = \phi_i + \hat{\phi}$ with interior flow v_i and interior density profile ρ_i and formulates equations for near-boundary deviations. Using a small angle approximation $(\sin(\theta) \cong \alpha, \cos(\theta) \cong 1)$, the equations for the boundary variables in a boundary normal coordinate $\hat{z}$ are (e.g. Brink and Lentz, 2010):

$$\frac{\partial \hat{u}}{\partial t} - f\hat{v} = \hat{b}\alpha + \frac{\partial}{\partial_{\hat{z}}} A \frac{\partial \hat{u}}{\partial_{\hat{z}}} \tag{6a}$$

$$\frac{\partial \hat{v}}{\partial t} + f\hat{u} = \frac{\partial}{\partial_{\hat{z}}} A \frac{\partial \hat{v}}{\partial_{\hat{z}}} \tag{6b}$$

$$\frac{\partial \hat{b}}{\partial t} + \hat{u}\, \alpha\, N^2 = \frac{\partial}{\partial_{\hat{z}}} K \frac{\partial \hat{b}}{\partial_{\hat{z}}} \tag{6c}$$

in which the interior buoyancy gradient, $N^2 = -g\rho_0^{-1}\rho_{iz}$ has been assumed constant. The fluxes $\overline{\mathbf{u}'\hat{\phi}'}$ have been represented by flux-gradient closure schemes. An important caveat is that the fluxes in (x, y, z) need not be isotropic (i.e. 3-dimensional). While this assumption may characterize grid generated turbulence that is the subject of the Phillips (1970) and Phillips et al. (1986) laboratory studies of boundary layers over sloping topography, motions characterizing turbulent fluxes over flat topography in geophysical systems are anisotropic (e.g. Kaimal et al., 1972): 3-d isotropic motions in boundary layers are inefficient at communicating the boundary conditions. Rather, such 3-d motions are part of the inertial subrange. The presence of a sloping boundary compounds the issue: the sloping boundary represents an opportunity to couple with a resonant internal waveband process in which the internal waveband flux has an aspect ratio characteristic of the bottom slope, sections 4.1 & 4.3. The authors agree that the one-dimensional model is a perfectly reasonable paradigm. The issues orbit around the interpretation of A and K in terms of representing physical processes, the possible conflation of Cartesian (x, y, z), bottom normal $(x, y, \hat{z})$ and isopcynal coordinates, and relevant length scales of boundary processes. The implications of such distinctions are regarded as a fundamental open question, section 5.

A focal point for the one-dimensional model is the question encapsulated in figure 2: 'are the turbulent processes that give rise to the boundary layer structure simply mixing unstratified water?' and, more generally, 'what are the processes that might ventilate the bottom mixed layer and renew the stratification?' Steady solutions to (6) hold some answers to this question. One can view this problem from the perspective in which there is no interior mean flow and the boundary layer structure is a response to turbulent mixing imposed as an enhanced diffusivity. Working from this perspective, Chris Garrett (Garrett, 1990, 1991; Garrett et al., 1993; Garrett, 2001) built on the prior theoretical work of Phillips (1970); Wunsch (1970); Thorpe (1987) to derive theoretical expressions and understanding of the steady-state flows that occur near a sloping boundary when the slope of the boundary is constant, the interior far-field stratification is constant, and for small-scale diffusivities and viscosities that are functions of only the slope-normal distance $\hat{z}$. Because of the one-dimensional nature of the imposed geometry and stratification, a mean diapycnal flow occurred only if the diffusivity well away from the boundary was non-zero, but Garrett was able to

shed considerable light on the largely self-cancelling transports up and down the slope.

These steady solutions have a natural height scale q^{-1} (Garrett, 1990):

$$q^4 = \frac{1}{4}\left[\frac{N^2 \sin^2(\theta)}{A(\hat{z}=0)K(\hat{z}=0)} + \frac{f^2}{A^2(\hat{z}=0)}\right].$$
(7)

For an unstratified ocean (7) returns the familiar Ekman result $q^{-1} \rightarrow \sqrt{2A/f}$. Equation (7) also provides insight into the relative roles of buoyancy mixing and friction in dictating the structure of the boundary layer: buoyancy effects become more important as $P_r s^2 \rightarrow 1$, in which $P_r = A/K$ is the turbulent Prandtl number and

$$s = \frac{N \sin(\theta)}{f}$$
(8)

is the slope Burger number, with $s \sim O(1)$ providing a meaningful quantification of what constitutes 'steeply sloping topography'.

Isopycnals dip into the boundary to meet the no-flux boundary condition on this height scale with a reduction of buoyancy, with the implication that buoyancy fluxes are reduced from what might be estimated from the farfield stratification. The stratification is *not* zero, as might be imagined for a steady state solution: these dipping isopycnals imply pressure gradients that support an upslope flow near the boundary, figure 4, that continually 'restratifies'. If the imposed diffusivity decreases with height, pressure gradients in the opposite direction arise and a bidirectional flow results aloft. This cross-slope flow serves to maintain the stratification and there is no intrinsic need to transport 'mixed water' off-slope. On the other hand, intrusions of mixed fluid into the interior associated with a convergence in cross-slope transport resulting from changes in slope and / or interior stratification are possible (e.g. Phillips et al., 1986; Kunze et al., 2012).

If the height scale over which $K(\hat{z})$ varies is larger than q^{-1}, this model sets an expectation that the turbulent buoyancy fluxes near the boundary are smaller than those aloft. This limit is so commonly invoked that the weakly stratified near boundary region has been labeled the Bottom Boundary Layer (BBL) and turbulent regions aloft referred to as the Stratified Mixing Layer (SML), figure 4, which also delineates regions having upslope and downslope transports. Ferrari et al. (2016) carry this argument to an extreme and assert that the no normal flux boundary condition (4c) requires the diapycnal flux to be zero, $\overline{w'\rho'}(\hat{z}=0) = 0$. The upslope/downslope dichotomy is central to theoretical developments in Section 3.3-3.2. In Section 5 we forward the suggestion that Ferrari et al. (2016)'s assertion that $\overline{w'\rho'}(\hat{z}=0) = 0$ results from assuming the fluxes giving rise to the turbulence are nearly isotropic and that the notion that the BBL hosts generally smaller buoyancy flux magnitudes than in the SML is in jeopardy.

A second view of this problem is one in which the mixing is driven by an overlying geostrophically balanced along slope flow (Trowbridge and Lentz, 1991; Lentz and Trowbridge, 1991; MacCready and Rhines, 1991, 1993; Garrett et al., 1993). The intent of this class of problems is slightly different: cross-slope transport results from a combination of mixing and cross-slope advection in the Ekman layer, defined as the height scale over which the bottom drag is deposited. The focal point here has been the character of the steady state solution, known as the arrested Ekman layer, in which the boundary layer grows to sufficient height that the geostrophic shear associated with mean isopcynal
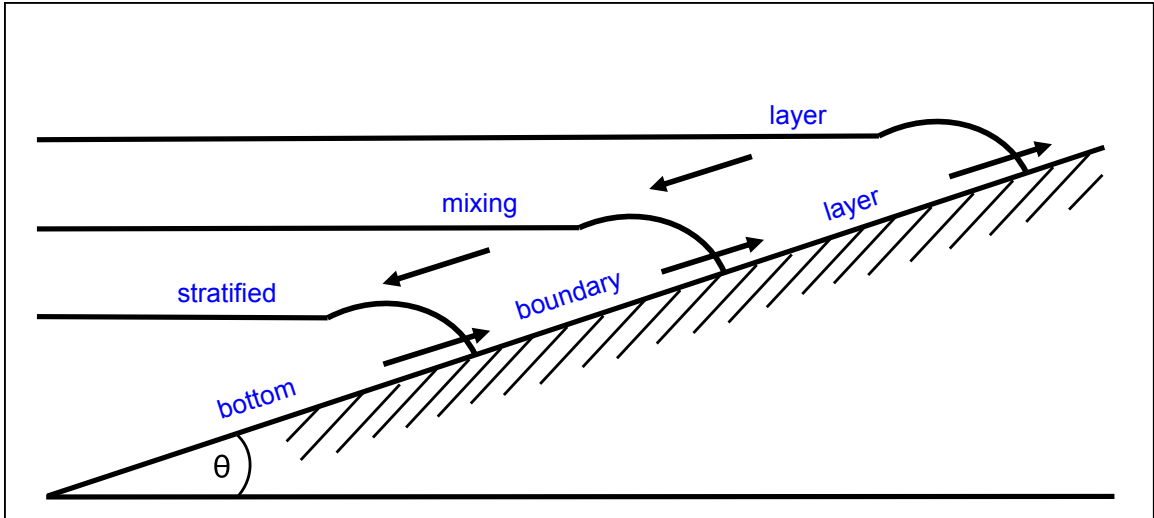
9

Figure 4: The basic one-dimensional model, featuring bidirectional flow as arrows crossing isopycnals that results from vertical structure in the mixing. The weakly stratified region near the boundary is dynamically distinct from a more strongly stratified region above. The near boundary region supports upwelling and is termed the bottom boundary layer (BBL), the more strongly stratified region supports downwelling and is termed the stratified mixing layer (SML). Adapted from Garrett (1991).

tilt decreases the bottom velocity, reduces the bottom stress, reducing mixing until the bottom velocity approaches zero. Early work on this problem is focused upon the slow time evolution ($\partial_t << f$) to the arrested state. This knowledge is acquired using a plethora of *ad hoc* assumptions about turbulent momentum and buoyancy fluxes via A and K with limited attempts to model the system with full-on closure schemes, (e.g. Weatherly and Martin, 1978). The work of Brink and Lentz (2010) and high performance computing (Umlauf et al., 2015; Ruan et al., 2019) opens up the examination of the time dependent problem using full-on turbulence closure schemes that address the potential for multiple height scales in the boundary layer and convective instabilities avoided in this early work. We attempt to summarize such efforts in section 4.

Density Coordinates

The transformation to a density coordinate system (McDougall, 1984, 1989; Marshall et al., 1999) provides a tremendous intellectual simplification: boundary mixing concerns the evolution of the buoyancy field in response to mixing, and transforming the equations of motion (1) into a density coordinate system (e.g Cushman-Roisin and Beckers, 2011) simplifies the density equation to a balance between time dependence, the divergence of the density flux and advection across isopycnals. It focuses attention directly upon diabatic processes and discards sub-inertial fluctuations that are quite efficient at dispersion along isopycnals but typically are not directly connected to 3-d turbulence and thus cause limited dispersion across isopycnals (e.g. Ferrari and Polzin, 2005). The mean diapycnal velocity is given by:

$$\tilde{\mathbf{e}} = -\frac{\nabla\cdot\mathbf{F}_\rho}{\|\nabla\rho\|}\mathbf{n}_\rho \tag{9}$$

and note that this expression applies even when the Eulerian fields are unsteady. This intellectual simplicity, though, comes at the cost of the analytic complexity of needing to include extra terms to allow for the curvature of isopycnal surfaces and the boundary conditions become much more complicated Garrett (2001)[4].

2.4 Integration

Integration is a vehicle for simplifying complex problems. This tool appears in three significant contexts.

Walin Style Control Volume Budgets

Using two surfaces of constant density as boundaries for a volume integral of the density equation leads to an expression for the time rate of change of volume V contained within those two isopycnals (Walin, 1982), figure 5:

$$\frac{\partial V}{\partial t} \ = \ -\frac{\partial G}{\partial \rho} + \Psi_{\text{advective}} \tag{10a}$$

$$G \ = \ \iint \tilde{\mathbf{e}} \, dA \tag{10b}$$

where G is the volume flux *across* an isopycnal maintained by turbulent processes. Ignoring inputs from geothermal sources and surface inputs, the transformation rate G is the area integrated diapycnal velocity from (9), dA is an infinitesimal area element and $\Psi_{\text{advective}}$ represents the advective fluxes of *intermediate* density into and out of the volume, such as those estimated by current meter arrays or geostrophic transport sections.

Hypsometry

The issue of integration exposes one to the fact that, along surfaces of constant depth, the area

$$A = \iint dA \tag{11}$$

is monotonically increasing as depth *decreases*. For example, $A(\rho_1) > A(\rho_2)$ in figure 5. This introduces a subtle interplay between increasing area with *decreasing* depth and the observed tendency of turbulent dissipation profiles to increase with *increasing* depth (figure 3 and Polzin et al. (1997)), implying a *local* (9) downwelling. The two trends compete in the Walin budget (10) and the net result, apart from a basin wide and global requirement for net upwelling, is not obvious. Upwelling requires that the area of isopycnals increase with height in such a way that even though the buoyancy flux decreases with height on each cast, the area integrated buoyancy flux increases with height (Klocker and McDougall, 2010). Specific proposals have been put forward in Polzin (2009) for single grid cells of a climate class GCM and for canyons incising larger scale sloping topography (Kunze et al., 2012; Thurnherr et al., 2020); see sections 3 and 5.

The Moment Method

---

[4]The inquisitive might note that the transformation from Cartesian into density coordinates assumes a one-to-one mapping between z and ρ and this is problematic in the case of convection, such as presented by a downwelling Ekman layer, section 4.3.

$$\frac{\partial V}{\partial t} = -\frac{\partial}{\partial \rho} \iint \tilde{\mathbf{e}} \, da + \Psi_{\text{advective}}$$
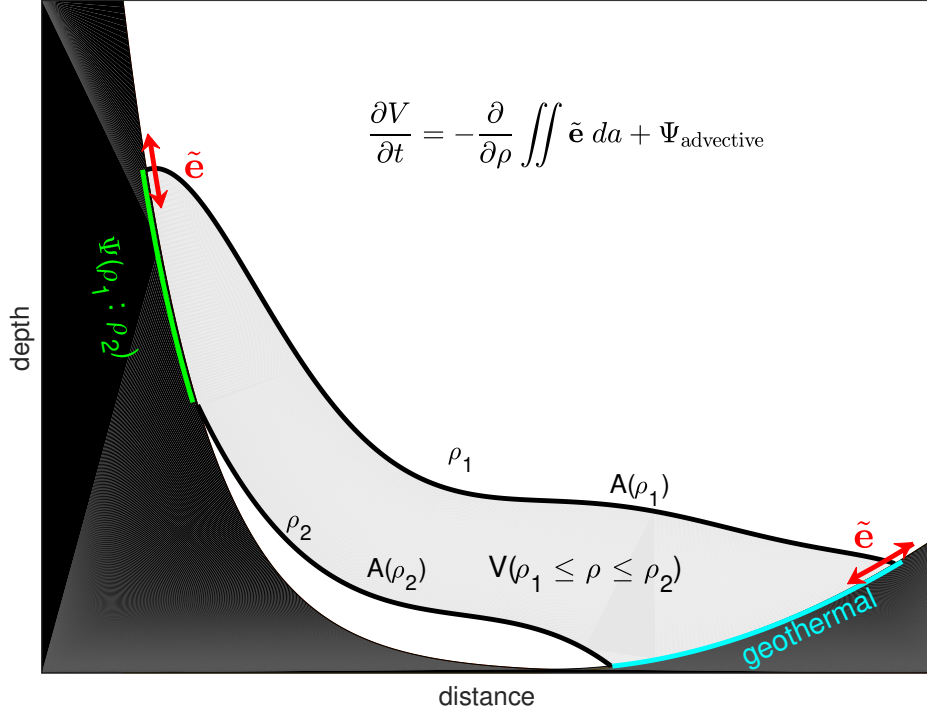
Figure 5: A schematic depiction of terms relating to the Walin budget (10) for the time rate of change of the volume V between two density horizons ρ_1 and ρ_2. The volume is indicate by the grey shaded area, mass and density Ψ is supplied on the left hand boundary via a gap in the side wall indicated by the green segment, diapycnal velocities $\tilde{\mathbf{e}}$, largest at the boundary, are indicated in red. The presence of geothermal heating, neglected in (10), is represented in cyan.

The moment method is a generic method for analyzing stochastic systems in a wide variety of contexts (Gardiner et al., 1985; Polzin and Lvov, 2017) involving dispersion. Given an equation for tracer concentration (3) and a closure such as (2), one multiplies the equation by a spatial coordinate, integrates over space and applies appropriate boundary conditions. For example, a delta function initial condition in a homogeneous ocean where the tracer never reaches the boundary leads to

$$\langle z^2 \rangle = 2 \, K \, t \tag{12}$$

in which $\langle z^2 \rangle$ is the mean squared dispersion about the center of mass. In mixing studies, such metrics are useful comparisons to estimates of tracer dispersion across isopycnal surfaces (Ledwell et al., 2000; Holmes et al., 2019). See section 3 for further discussion concerning boundary conditions.

2.5 Energetics and Mixing

The ability of turbulent production to result in a buoyancy flux is a significant part of the lexicon concerning ocean turbulence. How this plays out in the context of boundary mixing is central to some of our disagreements, and to address this we need to draw together basic (e.g. Tennekes and Lumley, 1972) statements about energy budgets and how measurements intersect with those budgets.

2.5.1 Energetics

We start from a Reynolds decomposition, multiply the equations of motion by their perturbations and time average:

TKE Equation
The equation for the time averaged turbulent kinetic energy $\overline{u_i' u_i'}/2 = TKE$ is:

$$\frac{1}{2}\left[\frac{\partial \overline{u_i' u_i'}}{\partial t} + \overline{u}_j \frac{\partial \overline{u_i' u_i'}}{\partial x_j}\right] + \overline{u_i' u_j' \frac{\partial \overline{u}_i + u_i'}{\partial x_j}} \;\cong\; -\rho_0^{-1}\frac{\partial}{\partial x_i}\overline{u_i' p'} + \overline{b' w'} - \frac{\nu}{2}\overline{\left(\frac{\partial u_i}{\partial x_j} + \frac{\partial u_j}{\partial x_i}\right)^2}$$

$$\frac{d}{dt}TKE \quad - \quad \mathcal{P}_k \;+\; N.L. \;\cong\; P_{\text{work}} \;+\; \mathcal{B} \;-\; \epsilon \tag{13}$$

Time rate of change of TKE following the mean flow $\overline{u}_j$ is balanced by turbulent production $\mathcal{P}_k$ and nonlinear transports, pressure work, buoyancy flux $\mathcal{B}$ and the kinetic energy dissipation rate ϵ. Terms of $O(\ell/L)^2 \ll 1$, in which ℓ is a metric of the strain (dissipation) field and L is the outer, energy containing scale of the turbulent velocity, have been neglected in comparison to the dissipation rate ϵ (Tennekes and Lumley, 1972). Here u_i are velocity vector components with vertical component $u_3 = w$, ν is kinematic viscosity and repeated indices imply summation.

Scalar Variance Equation
A similar slowly varying construct emerges for the scalar (here density ρ) variance equation:

$$\frac{1}{2}\left[\frac{\partial \overline{\rho_i' \rho_i'}}{\partial t} + \overline{u}_j \frac{\partial \overline{\rho_i' \rho_i'}}{\partial x_j}\right] \;+\; \overline{\rho' u_i' \frac{\partial \overline{\rho} + \rho'}{\partial x_i}} \;\cong\; -\frac{1}{2}\kappa \overline{\left(\frac{\partial \rho'}{\partial x_i}\right)\left(\frac{\partial \rho'}{\partial x_i}\right)}$$

$$\frac{d}{dt}SV/2 \quad - \quad \mathcal{P}_\rho \;+\; N.L. \;\cong\; - \quad \chi_\rho/2 \tag{14}$$

Time rate of change of the scalar variance SV is balanced by turbulent production $\mathcal{P}_\rho$, nonlinear transports and dissipation χ_ρ. Terms $O(\ell_\rho/L) < \ell/L \ll 1$, in which ℓ_ρ is a metric of the turbulent density gradient (dissipation) field, have been neglected in comparison to the rate of dissipation of density variance, as in (13). The *vertical* component of the density flux in (14) appears as a source of potential energy in (13). This distinction is a key issue in boundary mixing, section 5.[5]

2.5.2 Metrics of Mixing

The holy grail in the study of 'mixing' is, well, mixing, by which we mean the turbulent transport of a substance C, $\overline{\mathbf{u}'C'}$, across mean isopleths, $\overline{C}$, in (3) and (14). Direct measurement of the fluxes is

---

[5]We set aside questions concerning density being related to both temperature and salinity, considering the fluid to be temperature dominated and boundary mixing to be a turbulent stress or form drag driven paradigm.

quite difficult, hence the usual course of events is to argue from restricted balances of (13) and (14) and relate the fluxes, which happen at the overturning scales, to dissipation, which is the smallest turbulent scale.

This is a convoluted process. First, one assumes steady conditions, then asserts that integration of the triple correlations $\overline{u_i' u_j' \frac{\partial u_i'}{\partial x_j}}$ and $\overline{\rho' u_i' \frac{\partial \rho'}{\partial x_i}}$ over a volume and application of Green's theorem renders the triple correlations as the net turbulent transport across the volumetric boundaries, small for large volumes and negligible for spatially homogeneous conditions but yet potentially problematic near boundaries (Shaw et al., 2001), and finally pleads ignorance about the role of turbulent pressure-velocity correlations, fervently hoping that volumetric integration smooths away any issues. Second, one acknowledges the role of stratification in differentiating stirring along isopycnals by largely adiabatic motions from mixing across isopycnals by their diabatic brethren. This brings one to the turbulent production - dissipation balances advocated by Osborn (1980)

$$-\mathcal{P}_k \cong \mathcal{B} - \epsilon \tag{15}$$

and Osborn and Cox (Osborn and Cox, 1972)

$$\overline{\rho' w'} \, \overline{\rho}_z = -\chi_\rho / 2 \tag{16}$$

which further assumes production is dominated by vertical terms. The working hypothesis is that one can define a flux Richardson number as the ratio between the buoyancy flux and turbulent production:

$$R_f = -\frac{\mathcal{B}}{\mathcal{P}_k} \; . \tag{17}$$

With (15) and (16) one has two indirect routes to empirical knowledge of $\overline{\mathbf{u}'\rho'}$: via ϵ and via χ. Simultaneous knowledge of both provides a dissipation ratio,

$$\Gamma_\mu = \frac{\chi_\rho \, N^2}{\epsilon \, 2 \, \overline{\rho}_z^2} = \frac{R_f}{1 - R_f} \; . \tag{18}$$

Empirical constraints on Γ_μ are provided by microstructure sensors resolving the dissipation scales. A second route is possible for sufficiently energetic turbulence. Energetic turbulence is often characterized by a range of wavenumbers k that are much larger than those characterizing the large scales of turbulence and much smaller than those at which molecular dissipation acts. Within this range it is reasonable to assume that the downscale transports of energy ϵ (relating to triple correlations $\overline{u_i' u_j' \frac{\partial u_i'}{\partial x_j}}$) and scalar variance χ_ρ (relating to $\overline{\rho' u_i' \frac{\partial \rho'}{\partial x_i}}$) are the only dynamically relevant parameters. Dimensional analysis relates the kinetic energy and scalar spectra:

$$\begin{aligned} E_k(k) &\cong C_k \, \epsilon^{2/3} \, k^{-5/3} \\ &\text{and} \\ E_\rho(k) &\cong C_\rho \, \chi_\rho \, \epsilon^{-1/3} \, k^{-5/3} \; . \end{aligned}$$

Knowledge of the spectral density E_k and E_ρ thus provides mid-scale estimates of mixing given the constants of proportionality (Kaimal et al., 1972; Sreenivasan, 1995, 1996) and can be summarized as a spectral transport ratio Γ_{trans}:

$$\Gamma_{\text{trans}} = \frac{C_k}{C_\rho} \frac{E_\rho(k)N^2}{2\bar{\rho}_z^2 E_K(k)} \ . \tag{19}$$

Such estimates are referred to as 'inertial subrange' estimates and appear in (13) and (14) as triple correlations in the primed variables.

If we turn our eyes towards the issue of production in the TKE equation, there are at least three phenomenological end members: shear production (e.g. $-\overline{u'w'}\,\overline{u}_z$), for which Γ_μ and Γ_{trans} are less than 0.2; convection - implicit in (13) as either forcing or mean conditions such as a downwelling Ekman layer that maintain a condition of static instability and result in the conversion of gravitation potential energy $\overline{w'b'}$ and for which $\Gamma = -1.0$; and form drag, which appears as a boundary condition (section 2.2) and results in pressure gradients that force flow accelerations and hydraulic transitions with an indeterminate Γ assignment. See Gregg et al. (2018) for a review of lab measurements, direct numerical simulations of shear instabilities and oceanic microstructure data.

The presence of near-boundary upwelling in the one-dimensional model (figure 4) occurs in association with a relative minimum in the buoyancy flux as a function of $\hat{z}$. This minimum is part of the model construction: one assumes $K(\hat{z})$ and $A(\hat{z})$ and then solves for the buoyancy field. The two, in combination as (2), return the mid-depth minimum in buoyancy flux. There are substantive issues in support of this that can be expressed as structure in the mixing metrics Γ_μ and Γ_{trans}, with small values of Γ below the mid-depth minimum. These are issues of length scale suppression, time dependence and tertiary dependencies of Γ upon turbulent intensity and gradient Richardson number.

Length Scale Suppression

Neither dissipation range nor inertial subrange estimates of ϵ or χ are what we want, which is an estimate of the fluxes $(\overline{\mathbf{u}'\rho'})$ at the overturning scales. A tool for addressing links between dissipation scales and overturning scales can be developed by assuming that the important balance is one between the force of gravity, ensconced in the stratification N, and the inertial forces of turbulence, encapsulated in the downscale transfer rate in an inertial subrange, ϵ. Dimensional analysis leads to the Ozmidov length L_o,

$$L_o = \sqrt{\epsilon/N^3}$$

which can be compared to a direct estimate of overturning quantified as the root-mean-squared vertical displacement z' of parcels in an overturn (Thorpe, 1977) after sorting to be statically stable:

$$L_T = \overline{z'^2}^{1/2} \ .$$

The unbounded shear flow, for which $\Gamma \cong 0.2$, is a situation in which the overturning scales are free

15

to evolve such that $L_T \cong L_o$. The distance from the boundary represents a fundamental imposition of an external length scale that plausibly impacts mixing efficiency. It is directly expressed as wall layer scalings in turbulent closure schemes (e.g. Mellor and Yamada, 1974) with the suppression of turbulent length scales implying smaller gradient Richardson number R_i and smaller flux Richardson number R_f in association with smaller R_i. A reduction in mixing efficiency associated with length scale constraints is both fundamental and intuitive, but yet competes with increasing stress-driven dissipation as the boundary is approached and is fundamentally grounded in the paradigm of steady flow over a flat bottom.

Time Dependence

Internal wave breaking has a life-cycle between overturning and dissipation (Smyth et al., 2001; Chalamalla and Sarkar, 2015) that is expressed in L_T and L_o and impacts the interpretation of data. There is the potential for wave breaking to emphasize 'younger' parts of the life-cycle and support more efficient mixing.

Tertiary Dynamics

An ongoing source of uncertainty (e.g. Mashayek et al., 2017; Ijichi et al., 2020) is the potential of a tertiary dependence of Γ_μ upon either turbulent intensity,

$$R_{eb} = \epsilon/\nu N^2 \tag{20}$$

which is proportional to the ratio of overturning scales L_o to dissipation scales $L_k = (\epsilon/\nu^3)^{-1/4}$ and serves as a bandwidth for the inertial subrange, or upon gradient Richardson number R_i on scales relevant to overturning.

Having noted these details concerning mixing metrics, we remind ourselves about the source of knowledge for the mid-depth minimum in buoyancy flux: we have arrived at this via a mixing length closure that is appropriate for small perturbations in a steady flow that are related to the local gradients. The phenomenology of boundary mixing presented in section 4 is that of convection in an Ekman layer coupled with a resonant internal wave band process, episodic convection associated with an internal wave-breaking process and O(1) variations in stratification within the boundary layer on the internal wave time scale. None of this meshes well with a mixing length closure or the discard of transport terms in (13) and (14). Skepticism is required both here and in the interpretation of mixing metrics Γ via extrapolation of results from regions without boundaries to the issue of boundary mixing. Moreover, the internal wave band processes being emphasized have motions that parallel the slope. We remind ourselves that what we want in a discussion of boundary mixing are estimates of $\overline{\mathbf{u}'C'}$ in (3). This is *not* identical to the buoyancy flux $w'b'$ in the TKE equation (13), where the buoyancy flux enters only in the direction of gravity. With isopleths of C dipping into the boundary, these cross slope fluxes project across those mean isopleths. The propensity to ignore this distinction leads us to articulate an open question in section 5, where we call for more and better data to address these concerns.

3 Implications of the bottom intensification of ocean mixing for upwelling: buoyancy budgets for bottom-intensified mixing

In this section we are mainly concerned with understanding the area-integrated volume transports of water moving both downwards and upwards across density surfaces. The crucial statements are the diapycnal advection - diffusion balance (9) and corresponding budget for the volume of water contained between two isopycnals (10). Because there is no buoyancy flux through the sea floor, it is hard to avoid upwelling very close to a sloping ocean floor. The global response, though, is complicated by hypsometric considerations (11). In section 3.1 we discuss the impact that including such near-boundary mixing structure has for the global stratification in numerical models. In sections 3.2 through 3.5 we discuss and then dissect the details of solutions to the one-dimensional boundary layer problem posed in (6) that relate to this structure. We discuss aspects of the ventilation of the boundary by adiabatic processes (eddy-stirring) in 3.2 and touch upon the interpretation of tracer releases in light of such boundary layer structure in section 3.6. We return to comment upon the implications for the horizontal circulation in numerical models (section 3.7).

3.1 Abyssal ocean circulation models are sensitive to bottom topography

Ocean models have traditionally used a constant value of the diapycnal diffusivity, or at least a vertical profile that is essentially constant below a depth of 2000 m (Bryan and Lewis, 1979). With the stratification, $N^2 = b_z$, being an increasing function of height, a depth-independent diapycnal diffusivity implies that the dissipation of turbulent kinetic energy, ϵ, increases with height, in contrast with observations in the abyss (figure 3). General Circulation Models run with parameterizations of bottom enhanced mixing via increasing diffusivity with depth (e.g. Jayne, 2009; Melet et al., 2013) host vigorous overturning cells, implying a complex interaction between downwelling implied by increasing diffusivity with depth and changing stratification to permit greater net upwelling.

This complex interaction was explored in an idealized setting by specifying the buoyancy flux profile (Ferrari et al., 2016). The buoyancy flux profile was constructed so as to have a relative minimum at a height above bottom of 80 meters, and two variants of model topography were considered. One such model was constructed with a flat bottom and vertical walls. A steady state was reached, with sufficient "upwelling" along a thin boundary layer along the flat ocean bottom to overcome the diapycnal downwelling in the ocean interior. However, the model's interior stratification was much weaker than in the real ocean. When the model topography was re-configured with sloping side walls, a much more realistic stratification and meridional overturning circulation was obtained, again with diapycnal downwelling in the ocean interior and relatively fast upwelling in thin bottom boundary layers on the sloping boundaries. The diapycnal upwelling transport in these boundary layers was about 2.5 times the net diapycnal upwelling, with the balance (-1.5) sinking across isopycnals in the ocean interior. The pattern of near-boundary upwelling and downwelling relates directly to that in the one-dimensional model presented in section 2.3. The net (global) upwelling (10) then relates to basin geometry through hypsometric arguements (11).

Using World Ocean Circulation Experiment data, conventional topography and mixing specified through a diffusivity profile, de Lavergne et al. (2016b) diagnose negative diapycnal transports in the ocean interior and emphasize the substantial upwards vertical transport in the bottom boundary layer, with the latter resulting from the convergence of the turbulent flux of buoyancy resulting from adjustments (weakening) of the BBL stratification and due to geothermal heating. de Lavergne et al. (2017) find that the maximum in the meridional overturning streamfunction is insensitive to how abyssal mixing is specified in terms of various geophysical parameters (e.g. topographic slope, abyssal height variance, etc.) and in so doing make a reasonably strong statement that global hypsometry controls the maximum in the meriodional overturning stream function.

The study of Ferrari et al. (2016) showed that when the buoyancy flux of small-scale mixing is forced to decrease with height in an ocean model, the deep circulation is very sensitive to the bottom topography, with the deep circulation being completely different when the topography consisted of vertical walls and a flat bottom, versus having more realistic non-vertical and non-horizontal topography. This sensitivity is not apparent when the magnitude of the diapycnal buoyancy flux of small-scale mixing is allowed to increase with height, thus allowing upwelling in the ocean interior. This sensitivity of the abyssal circulation to the bottom topography (the ocean's hypsometry) will be taken up again in section 3.4 below.

3.2 One-dimensional solutions for flow near a sloping bottom boundary

Callies (2018) has shown that for oceanographically relevant parameters of the earth's rotation, abyssal boundary slopes, and the small-scale diffusivity and viscosity; the vertical stratification that is predicted by these one-dimensional near-boundary solutions is very weak, and he suggested that the sloping isopycnals that are typical of these solutions are unstable to baroclinic instability, and that including the resultant adiabatic stirring of the thickness between closely spaced density surfaces (Gent et al., 1995; McDougall and McIntosh, 2001) makes a material difference to the stratification. Naveira Garabato et al. (2019) have observed this type of adiabatic submesoscale eddy exchange in an abyssal boundary current in the Orkney Passage, finding evidence of both symmetric and centrifugal instabilities along with enhanced diapycnal mixing. One way of parameterizing this bolus transport is as a greatly increased vertical viscosity and Prandtl number, following the work of Greatbatch and Lamb (1990). With this modification, the one-dimensional near-boundary flow model of Garrett (1990, 1991, 2001) gives the steady-state Bottom Boundary Layer (BBL), being the region closest to the sloping wall where the flow is upslope, to be a few tens of metres thick. The upward flow is concentrated in the lowermost third of this distance where the stratification is weak (see Figure 6), while the upper half of the BBL is well stratified (Holmes and McDougall, 2020).

3.3 Expressions for the upwelling in the BBL and downwelling in the SML

Consider a one-dimensional situation with the ocean floor sloping at an angle with respect to the isopycnals lying above the boundary layer region, and with the far-field stratification $N^2 = b_z$ being depth-independent (where $b = -g(\rho - \rho_{\text{bottom}})/\rho_{\text{bottom}}$ is the buoyancy and ρ_{bottom} is the density
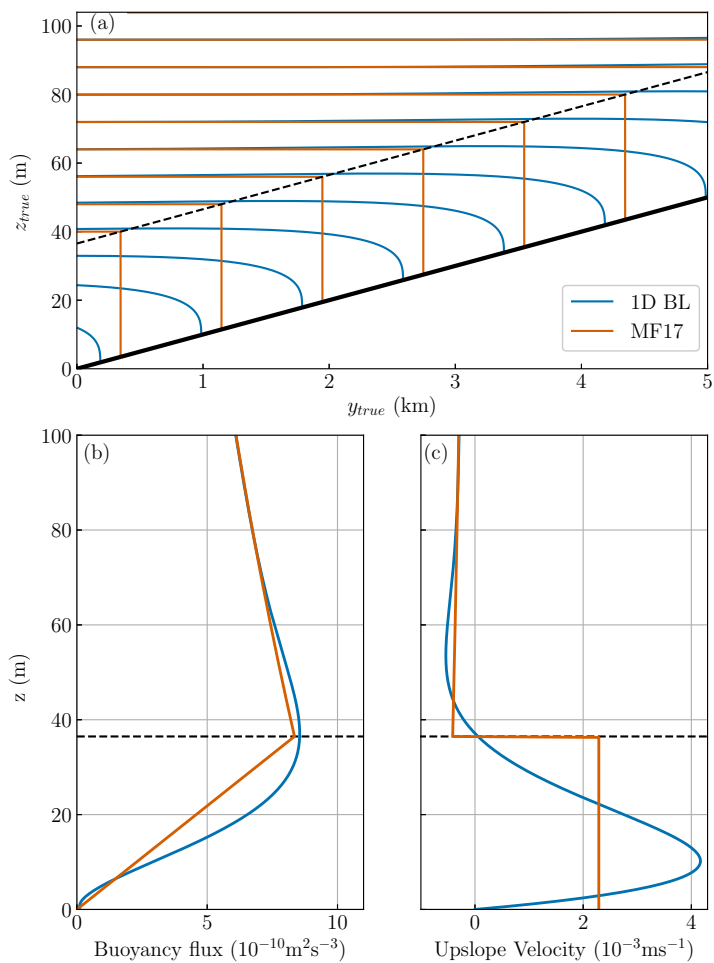
Figure 6: (a) Cross-section of isopycnals (smooth blue contours) in Garrett's one-dimensional (1D) boundary layer solution in the vertical plane, with the horizontal axis being up-slope distance. The dashed black line separates the downward-flowing stratified mixing layer SML from the upward-flowing bottom boundary layer (BBL). (b) The magnitude of the diffusive buoyancy flux (smooth blue line) of the 1D solution, which has a maximum value at the top of the BBL. (c) The upslope velocity as a function of distance normal to the boundary. In these panels the full blue lines are for the 1D boundary layer solution, while the full yellow lines are for McDougall and Ferrari (2017)'s assumed geometry in which the interior has a constant stratification, the BBL is well mixed, and the turbulent buoyancy flux in the BBL varies linearly with height.

at the densest part of the ocean); figure 6. The slope-normal coordinate is designated $\hat{z}$ and the magnitude of the small-scale turbulent diapycnal buoyancy flux per unit area is written as a function of $\hat{z}$ as $\mathcal{B}(\hat{z})$. Considering bottom-intensified mixing, and ignoring for now the background diapycnal diffusion in the ocean interior, we take $\mathcal{B}(\hat{z})$ to decay to zero at large distance from the sea floor, while right at the sea floor, the component of the buoyancy flux normal to the boundary must be zero (apart from the geothermal heat flux coming through the sea floor). As $\mathcal{B}(\hat{z})$ increases downwards towards the sea floor, it reaches a maximum value, $\mathcal{B}_0$, before decreasing towards zero at the sea floor.

At the height of the maximum magnitude of the turbulent buoyancy flux, $\mathcal{B}_{\hat{z}}$ is zero and so the diapycnal velocity is zero. Between the sea floor and the height at which $\mathcal{B}(\hat{z})$ reaches its maximum value $\mathcal{B}_0$, the diapycnal velocity is positive, moving up-slope (in a steady-state) towards less dense water, while above this height the diapycnal velocity is negative and the fluid flows parallel to the sea floor in the direction towards denser fluid. Following Ferrari et al. (2016) and McDougall and Ferrari (2017) we label the region close to the sea floor where fluid upwells towards less dense seawater the Bottom Boundary Layer (BBL) of thickness h and the fluid immediately above this, where the diapycnal velocity is negative, is called the Stratified Mixing Layer (SML). We expect the BBL to occupy the region within a few tens of metres above the sea floor, while the e-folding vertical distance of the SML is expected to be between 200 m and 500 m (Callies, 2018).

The buoyancy budget for the fluid in the BBL shows that the (positive) diapycnal volume transport towards less dense fluid is given by (McDougall and Ferrari, 2017; Holmes and McDougall, 2020):

$$\mathcal{E}_{BBL} = \int \frac{\mathcal{B}_0}{|\nabla b|} \frac{1}{\tan(\theta + \psi)} dx \; , \qquad (21)$$

where $|\nabla b|$ is the magnitude of the spatial gradient of buoyancy at the top of the BBL, and $(\theta + \psi)$ is the angle between the sea floor and the isopycnals at the height of the top of the BBL (with θ being the angle between the horizontal and the sea floor and ψ the angle between the horizontal and the isopycnal surfaces). Here the integral is taken horizontally along the incrop line (into the page) where the isopycnal intersects the sea floor. Taking $\mathcal{B}_0 = D_0|\nabla b|$ to be the product of $|\nabla b|$ and the diffusivity at the top of the BBL, D_0, this equation simplifies to

$$\mathcal{E}_{BBL} = \int \frac{D_0}{\tan(\theta + \psi)} dx \; . \qquad (22)$$

In deriving these expressions the effect that the non-linearity of the equation of state of seawater has on the relationship between upwelling and the divergence of the buoyancy flux has been ignored. Also, in assuming one-dimensional geometry and constant far-field stratification we have ignored any variation up the slope of the turbulent diffusive flux of buoyancy across successive buoyancy surfaces inside the BBL, F_{BBL}; Holmes and McDougall (2020) have derived the additional term that appears in the above equations (their equation (14)) when such upslope variation is present.

The expression (22) states that the upwards diapycnal transport in the BBL per unit horizontal distance along the isopycnal incrop line is $D_0/\tan(\theta + \psi)$, where $\tan(\theta + \psi)$ is the tangent of the angle that isopycnals at the top of the BBL make with respect to this upper boundary of the BBL.

With a constant height h of the BBL, this is the same angle that these isopycnals at the top of the BBL make with respect to the sloping sea floor. The need for this transport to be proportional to the diffusivity at the top of the BBL, D_0, is understandable, and the reason for the division by $\tan(\theta + \psi)$ arises because (i) the up-slope buoyancy gradient along the top of the BBL is smaller than $|\nabla b|$ by the factor $\sin(\theta + \psi)$, and (ii) the component of the diapycnal buoyancy flux per unit area normal to the top of the BBL is smaller than $\mathcal{B}_0 = D_0|\nabla b|$ by the factor $\cos(\theta + \psi)$.

Applying the Walin (1982) type buoyancy budget analysis (10) to the whole volume between a pair of closely spaced buoyancy surfaces, and continuing to ignore the geothermal buoyancy flux, the area-integrated, or net, volume transport upwelling though a buoyancy surface is given by

$$\mathcal{E}_{net} = \mathcal{E}_{BBL} + \mathcal{E}_{SML} = \frac{dF}{db} \ , \tag{23}$$

where the net upwelling $\mathcal{E}_{net}$ (in m^3 s^{-1}) is the sum of the upwelling in the BBL, $\mathcal{E}_{BBL}$, and that in the SML, $\mathcal{E}_{SML}$, which is negative. Here the turbulent buoyancy flux across the whole area of an isopycnal is here defined as

$$F = F_{BBL} + F_{SML} = \int \int \mathcal{B}(b, x, y) dx dy \tag{24}$$

where it is recognized that there are contributions to F from both the SML and the BBL.

In order to develop an expression for the sinking volume transport through buoyancy surfaces in the SML, $\mathcal{E}_{SML}$, the magnitude of the vertical component of the turbulent diapycnal buoyancy flux is taken to be an exponentially decreasing function of buoyancy, $\mathcal{B}(b, x, y) = \mathcal{B}_0(x, y)e^{-(b-b_0)/\Delta b}$, with the e-folding buoyancy scale being Δb, and $\mathcal{B}_0(x, y)$ being the turbulent buoyancy flux at the height of the boundary between the BBL and the SML. The exactly vertical velocity through buoyancy surfaces (often denoted with the symbol e) is $\partial \mathcal{B}/\partial b|_{x,y} = -\mathcal{B}(x, y, b)/\Delta b$, and when this is area-integrated along an isopycnal over the full area of the SML we find that

$$\mathcal{E}_{SML} = -\frac{1}{\Delta b} \int \int_{SML} \mathcal{B}(b, x, y) dx dy = -\frac{F_{SML}}{\Delta b} = -\frac{F_{SML}}{N^2 d} \tag{25}$$

where we have assumed that the e-folding buoyancy scale Δb does not vary with horizontal location along the buoyancy surface in the SML region, and in the last part of Eqn. (25) we have replaced the buoyancy scale Δb with an e-folding vertical distance d (which is often taken to be 500 m) and the square of a buoyancy frequency that is typical of the SML region along this isopycnal. When the e-folding height d of the turbulent buoyancy flux is much larger than the thickness of the BBL h, the contribution of the BBL to the area-integrated buoyancy flux F is small, so that in this case $F = F_{BBL} + F_{SML} \approx F_{SML}$. From Holmes and McDougall (2020) we expect F_{BBL}/F to be 0.05.

Just as the diapycnal upwelling in the BBL increases as the tangent of the angle between isopycnals and the sea floor, $\tan(\theta + \psi)$, decreases (as we noted from Eqn. (22)), so too does the magnitude of the downwelling in the SML, because for smaller values of $\tan(\theta + \psi)$ the area of the integral where $\mathcal{B}(b, x, y)$ is significant expands.

3.4 How much larger is the upwelling in the BBL than the net upwelling?

The horizontally uniform upwelling paradigm of Munk (1966) and Munk and Wunsch (1998) has held sway for so long, and with the dynamical implications of bottom-intensified ocean mixing only now beginning to be understood, it is perhaps too early to expect that a simple paradigm might emerge to replace the horizontally uniform view. If such a simple paradigm does emerge, it will likely rely on the implications of a Walin (1982) type buoyancy budget. The example of a conical ocean with the magnitude of the turbulent buoyancy flux at the top of the BBL $\mathcal{B}_0$ being constant, might serve as an example of an alternative paradigm to the one-dimensional upwelling-diffusion model; not that we think that a conical ocean is very realistic. A conical ocean has a constant slope $\tan\theta$ with the radius R of the ocean increasing with height according to $R_z = 1/\tan\theta$. Applying the overall buoyancy budget, Eqn. (23), shows that for heights well above the deepest part of the ocean, the net diapycnal upwelling transport is (from section 7 of McDougall and Ferrari (2017))

$$\mathcal{E}_{net} = \frac{\mathrm{d}F}{\mathrm{d}b} = D_0 \frac{2\pi d}{(\tan\theta)^2} \qquad \text{(conical ocean)}, \qquad (26)$$

where the e-folding height scale d of the magnitude of the turbulent buoyancy flux has been assumed to be much larger than the thickness of the BBL, h, and the isopycnals have been assumed to be horizontal outside the BBL. This expression can be understood by noting that the area of the SML scales as $R2\pi d/\tan\theta$ and when this is vertically differentiated, the second negative power of $\tan\theta$ enters since $R_z = 1/\tan\theta$. The ratio of the upwelling volume flux in the BBL to $\mathcal{E}_{\text{net}}$ in this conical ocean is given by (using Eqn. (22))

$$\frac{\mathcal{E}_{\text{BBL}}}{\mathcal{E}_{net}} = \frac{R\tan\theta}{d} \qquad \text{(conical ocean)}, \qquad (27)$$

From these relations we see that (i) the net upwelling of Bottom Water, $\mathcal{E}_{net}$, is independent of the radius R of the cone, so that the same net volume flux $\mathcal{E}_{net}$ upwells through all height levels of the conical ocean, and (ii), both $\mathcal{E}_{BBL}$ and $|\mathcal{E}_{SML}|$ are significantly larger than $\mathcal{E}_{net}$, and they both increase linearly with R, that is, they increase linearly with height (see figure 7). Holmes et al. (2018) have explored the implications for upwelling in the BBL and downwelling in the SML of many idealized situations with variable topography and variable stratification.
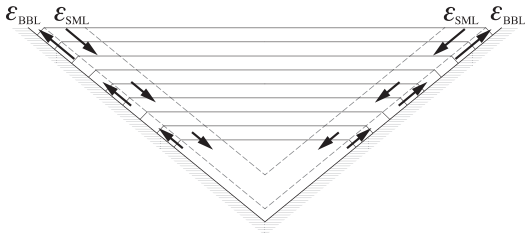

Figure 7: An ocean with conical bottom topography and a constant value of the diffusive buoyancy flux at the top of the bottom boundary layer (BBL). The magnitudes of the diapycnal transports in both the BBL and the SML increase with height, while the diapycnal velocities in both the BBL and the SML are independent of height (if the vertical interior stratification is depth-independent).

More generally, we can gain some insight into the ratio of $\mathcal{E}_{BBL}$ to $\mathcal{E}_{\text{net}}$ by essentially regarding

the variation of $\mathcal{E}_{\mathrm{net}}$ with buoyancy, $\mathcal{E}_{\mathrm{net}}(b)$, as known, and by integrating Eqn. (23) we find that

$$F = F_{BBL} + F_{SML} = \int_{b_{\min}}^{b} \mathcal{E}_{\mathrm{net}} db' \ , \tag{28}$$

where the integral is performed from the very densest water with buoyancy $b_{\min}$. From Eqns. (25) and (28) we find that

$$\mathcal{E}_{SML} = -\frac{F_{SML}}{F} \frac{1}{N^2 d} \int_{b_{\min}}^{b} \mathcal{E}_{\mathrm{net}} db' \ , \tag{29}$$

McDougall and Ferrari (2017) took the BBL to be a well mixed boundary layer so that F_{BBL} was very small and the ratio F_{SML}/F was very close to unity. More realistically, Holmes and McDougall (2020) derived an expression for F_{BBL} in the one-dimensional near-boundary formulation, finding that F_{BBL}/F is approximately $1.4/\pi$ times the ratio of the relevant vertical length scales, that is, $F_{BBL}/F \approx 0.45 h/d$, where h is the thickness of the BBL, and taking h/d to be 0.1, we expect F_{SML}/F to be approximately 0.95. The expression for the ratio of $\mathcal{E}_{BBL}$ to $\mathcal{E}_{net}$ is found from Eqn. (29) together with the additive relation, $\mathcal{E}_{net} = \mathcal{E}_{BBL} + \mathcal{E}_{SML}$, obtaining

$$\frac{\mathcal{E}_{BBL}}{\mathcal{E}_{net}} = 1 + \frac{F_{SML}}{F} \frac{1}{\mathcal{E}_{net}} \frac{1}{N^2 d} \int_{b_{\min}}^{b} \mathcal{E}_{\mathrm{net}} db' \ , \tag{30}$$

This ratio of the upwelling in the BBL to the net diapycnal transport might be called an amplification factor, and this equation is a handy relationship for this amplification factor in terms of a vertical integral of the net upwelling transport. For example, Eqn. (30) shows that in the very densest parts of the world ocean, the diapycnal transport occurs mainly in the BBL with negligible sinking in the SML (from Eqn. (30) with $b \approx b_{\min}$). If the net upwelling transport, $\mathcal{E}_{\mathrm{net}}$, is assumed to be independent of buoyancy (or height), then for a typical value of N^2 of 1×10^{-6} s^{-2} at a depth of 2500 m where $b - b_{\min} \approx 2.5 \times 10^{-3}$ m s^{-2}, and with $d = 475$ m, Eqn. (30) requires the upwelling in the BBL, $\mathcal{E}_{BBL}$, to be $6\mathcal{E}_{\mathrm{net}}$ and the sinking diapycnal transport in the SML to be $-5\mathcal{E}_{\mathrm{net}}$. For example, if the net upwelling transport at this depth is 25 Sv, then the sinking transport in the SML is 125 Sv while 150 Sv is upwelled in the BBL.

It seems more realistic to assume that the net upwelling transport is a linear function of buoyancy, and under this assumption, Eqn. (30) requires that at a depth of 2500 m $\mathcal{E}_{BBL} = 3.5\mathcal{E}_{net}$ and $\mathcal{E}_{SML} = -2.5\mathcal{E}_{net}$. For example, if the net upwelling transport at this depth is 25 Sv, then the sinking transport in the SML is 62 Sv while 87 Sv is upwelled in the BBL. Using the Nikurashin and Ferrari (2013) parameterization of breaking internal waves in realistic topography, Ferrari et al. (2016) evaluated $\mathcal{E}_{BBL}$, $\mathcal{E}_{SML}$ and $\mathcal{E}_{net}$ as functions of buoyancy, finding $\mathcal{E}_{BBL}/\mathcal{E}_{net} \approx 3.8$ at a Neutral Density of 28.1 kg m^3, while McDougall and Ferrari (2017) applied Eqn. (30) to the net upwelling transport $\mathcal{E}_{net}(b)$ of the Lumpkin and Speer (2007) inverse study, finding $\mathcal{E}_{BBL}/\mathcal{E}_{net} \approx 6$ at the same Neutral Density value. Yet another estimate of $\mathcal{E}_{BBL}/\mathcal{E}_{net}$ can be found from the work of de Lavergne et al. (2017) where the integral in Eqn. (30) can be estimated from Figure 5c of that paper, yielding $\mathcal{E}_{BBL}/\mathcal{E}_{net} \approx 2$ at a Neutral Density of 28.11 kg m^3, so that, taking the net upwelling transport at this depth to be 25 Sv, the sinking transport in the SML is 25 Sv while 50

Sv is upwelled in the BBL.

The above estimates of the ratio $\mathcal{E}_{BBL}/\mathcal{E}_{net}$ vary between 2 and 6 in the abyssal ocean, and in our view, values between 2 and 4 are realistic estimates. Using this range of values for $\mathcal{E}_{BBL}/\mathcal{E}_{net}$, and with the net upwelling transport at this depth estimated at 25 Sv, the sinking transport in the SML is estimated to be between 25 Sv and 75 Sv, while between 50 Sv and 100 Sv is upwelled in the BBL.

In the present paradigm, much of the ocean interior is close to being adiabatic, while there is strong diapycnal upwelling occurring hard against the sloping bottom in a BBL that is only tens of metres thick. Taking an average bottom slope of 1/400, the BBL extends only ∼20km horizontally, and then there is a broader region of substantial diapycnal sinking in the SML whose thickness is about 500 m, and which has a horizontal width of ∼200 km. This view of the diapycnal transport where all of the upwelling occurs in narrow BBLs within ∼20 km horizontally of rough topography, stands in stark contrast to the previously assumed horizontally uniform upwelling.

In the above discussion of bottom-intensified mixing we have ignored (i) the geothermal buoyancy flux, (ii) a small constant background diffusivity of 1×10^{-5} m^2 s^{-1}, and (iii) the effects of the nonlinearities of the equation of state. The geothermal buoyancy flux arrives directly in the BBL and is estimated to cause an additional ∼ 4-8 Sv of diapycnal upwelling in the BBL (de Lavergne et al., 2016a).

A background diapycnal diffusivity of 1×10^{-5} m^2 s^{-1} causes an upwelling diapycnal volume flux of ∼ 2.5 Sv, with only a small part being in the BBL (McDougall and Ferrari, 2017), while the cabbeling and thermobaric dianeutral advection processes (caused by lateral mixing and the nonlinear nature of the equation of state) are thought to cause a diapycnal sinking transport of approximately this same amount (∼ 2.5 Sv) in the ocean interior (Iudicone et al., 2008) and (Klocker and McDougall, 2010). We conclude that the net diapycnal volume transport caused by a background diapycnal diffusivity, while small, is probably counteracted by the sinking through isopycnals caused by cabbeling and thermobaricity.

A separate type of nonlinear equation of state effect arises in the parameterization of the diapycnal buoyancy flux and its divergence. Since density and buoyancy are not conservative variables, the material derivative of buoyancy is not only caused by the divergence of the turbulent diffusive flux of buoyancy (as we have assumed in this article), but there are additional terms due to the spatial variation of the thermal expansion and saline contraction coefficients. This issue has been discussed in McDougall (1984); Klocker and McDougall (2010); IOC (2010); de Lavergne et al. (2016b), where it was found to be of leading order in the upper 1500 m of the ocean, but we do not mention it further here.

3.5 Net upwelling in the abyss depends mainly on the shape of the ocean floor

In order for there to be net upwelling of water through isopycnals, the area-integrated buoyancy flux F needs to increase with buoyancy (since from Eqn. (23), $\mathcal{E}_{net} = \mathrm{d}F/\mathrm{d}b$). For bottom-intensified mixing characterized by a vertical decay scale d, the area of active mixing on each isopycnal, A_{mix},

scales as the horizontal width $d/\tan\theta$ times the perimeter L of the isopycnal along the topography. Hence $F \sim \mathcal{B}_0 A_{mix} \sim \mathcal{B}_0 L d/\tan\theta$ so that $F^{-1}\mathrm{d}F/\mathrm{d}b$ scales as

$$\frac{1}{F}\frac{\mathrm{d}F}{\mathrm{d}b} \sim \frac{(\mathcal{B}_0)_b}{\mathcal{B}_0} + \frac{(A_{mix})_b}{A_{mix}} \sim \frac{(\mathcal{B}_0)_b}{\mathcal{B}_0} + \frac{(L)_b}{L} - \frac{(\tan\theta)_b}{\tan\theta} + \frac{d_b}{d} \ . \tag{31}$$

This suggests that there are four different ways that net upwelling can be enabled, namely (i) if the magnitude of the buoyancy flux at the top of the BBL, $\mathcal{B}_0$, is an increasing function of buoyancy, (ii) if the length (perimeter) L is an increasing function of buoyancy, (iii) if the slope of the sea floor $\tan\theta$ is a decreasing function of buoyancy, and (iv) if the vertical length scale d is an increasing function of buoyancy. de Lavergne et al. (2017) have implemented a wide variety of mixing scenarios and with each have evaluated the area-integrated buoyancy flux F along neutral density surfaces of a hydrographic atlas, paying attention to the ocean floor topography. From F as a function of buoyancy, the net upwelling rate $\mathcal{E}_{net} = \mathrm{d}F/\mathrm{d}b$ was calculated as a function of buoyancy, and de Lavergne et al. (2017) found that this upwelling $\mathcal{E}_{net}(b)$ in the abyss was quite insensitive to the choice of mixing scenario. Similar shapes for $\mathcal{E}_{net}(b)$ were found for bottom intensified mixing as for geothermal heating (which has the same implications for diapycnal transports as a vertical profile of constant turbulent buoyancy flux which goes to zero abruptly at the sea floor).

The reason for this behaviour is the dominance of the topography of the sea floor in the calculation of $\mathcal{E}_{net}(b)$. In the case of bottom intensified mixing, the second and third terms on the right-hand side of Eqn. (31) together represent the effect of sea floor geometry (with respect to density coordinates), and these terms were found to dominate Eqn. (31) in the abyss. With bottom intensified mixing, an isopycnal that has a larger area close to the sea floor is exposed to a larger area-integrated turbulent buoyancy flux than one that has a smaller area close to the bottom. This idea is encapsulated in the term "incrop area" which is the area of the sea floor that is seen by fluid within a small range of density between one density value and the next, so that "incrop area" has dimensions of area per unit buoyancy difference. de Lavergne et al. (2017) found that the "incrop area", $(A_{mix})_b$, was well correlated with the net upwelling transport $\mathcal{E}_{net} = \mathrm{d}F/\mathrm{d}b$ in the abyss, and this relationship held for a wide range of parameterized mixing scenarios. This finding was confirmed in the study by Holmes et al. (2018) where it was found that below a depth of 4500 m the change with buoyancy of the perimeter where Neutral Density surfaces intersect the sea floor dominates the calculation of the net diapycnal upwelling, while shallower than this 4500 m depth the incrop area decreases with height, implying that in this depth range, the only way to achieve net upwelling is by $\mathcal{B}_0$ increasing with buoyancy (the first term in Eqn. (31)), or by geothermal heating (which has the same transport implications as an interior buoyancy flux profile that does not change with height above the BBL).

This study by de Lavergne et al. (2017) also strongly points to the need to think of $\mathcal{E}_{net}(b)$ increasing strongly with buoyancy in the abyss rather than being a constant net upwelling transport. This, plus the strong influence of the sea floor topography ("incrop area" $(A_{mix})_b$) on the shape of $\mathcal{E}_{net}(b)$, and the relative insensitivity to the mixing scenario, represent strong contrasts to the one-dimensional, horizontally uniform, upwelling-diffusion paradigm.

3.6 What can be learned from purposefully released tracers?

In the above we have concentrated on understanding the implications of the bottom intensification of ocean mixing for driving the net diapycnal upwelling $\mathcal{E}_{net}$ in the deep ocean, as well as on estimating how much larger than $\mathcal{E}_{net}$ is the upwelling $\mathcal{E}_{BBL}$ that occurs in the thin bottom boundary layers. Given the diapycnal upwelling and downwelling that occurs near the sloping sea floor, one wonders what imprint this motion might have on the distribution of tracers in the ocean. Holmes et al. (2019) have taken some initial steps in understanding this problem, concentrating their investigations on a tracer that is purposely released either in the BBL or just above it in the SML, and using the velocity field of the one-dimensional boundary layer theory of Garrett (1990, 1991) and Callies and Ferrari (2018).

The tool here is conceptually straightforward. Given observations of a tracer $C(x, y, \rho, t)$ released on an isopycnal surface $\rho(t_0)$, the effort is to interpret the time evolving dispersion and mean drift of the tracer concentration about $\rho(t_0)$ in terms of the diapycnal mixing K. The simplest situation in which K is spatially uniform is given by (12). If $K = K(\rho)$ and is independent of (x, y), the first moment is proportional to $\partial K/\partial\rho$ (Ledwell et al., 1998). With boundary mixing there is the potential for the transfer of tracer into and out of boundary layers along isopycnals as well as the complications of boundary conditions (4) to consider. A conceptually straightforward tool has attained a potentially complicated interpretation.

When their tracer was released in the BBL its centre of mass moves strongly upwards to greater buoyancies while simultaneously, its diapycnal spread, as estimated from the rate of increase of tracer variance in buoyancy space, is much less than would be suggested by simply averaging the diapycnal diffusivity over the tracer patch. The reduction in the diapycnal spreading of the tracer occurs because the tracer is constrained to not diffuse through the sea floor, and also by the dipole of upwelling in the BBL and downwelling in the SML. When the tracer is injected in the SML its centre of gravity initially moves with the fluid downwards to greater densities.

The diapycnal diffusion of tracers in this near-boundary situation is also sensitive to the presence of along-isopycnal diffusion, or equivalently, to the intermittent exchange of fluid out of and into the near-boundary region, as emphasized by Armi (1979b). Suffice it to say that the diapycnal movement and diffusion of a tracer through the upwelling and downwelling regimes of the near-boundary flows, is very complicated, especially in the presence of lateral exchanges along isopycnals. What is clear from the initial work in this area by Holmes et al. (2019) is that, for a purposefully released tracer in the BBL, it is not uncommon for the actual tracer-weighted diapycnal diffusivity to be three times as large as would be naively estimated by examining the rate of change of the tracer variance in buoyancy space.

3.7 Implications for the circulation of the abyssal ocean

Stommel and Arons (1959) posited a spatially uniform vertical velocity at mid-depth as the cause of vertical stretching of water columns in the deep ocean interior that drives the abyssal circulation through the linear vorticity equation. At first blush there would seem to be a problem with the sign of the interior Stommel-Arons abyssal circulation, simply by realizing that as the dense plumes

of Antarctic Bottom Water sink into the abyss, they are traditionally assumed to entrain and thus increase their volume flux as they descend to the deepest part of the ocean. As pointed out by McDougall (1989) and by Rhines (1993), because of this increasing volume transport with depth, and more importantly, also due to the decreasing ocean area as a function of depth, the average vertical velocity across successive heights, required simply by continuity, is a decreasing function of height, which is the opposite of the assumed stretching of water columns in the Stommel-Arons theory. The resolution of this conundrum will likely rely on the work of Baines (2001, 2005) and Hogg et al. (2017) which shows that dense gravity currents do not always entrain fluid from the environment as they make their way to the sea floor. Rather, on sufficiently weak slopes, descending plumes detrain fluid into the environment.

In thinking about diapycnal motion across isopycnals in the abyssal ocean it is useful to first imagine an isopycnal to be essentially at constant height. This then leaves a small area at this height that is not of the same density as the isopycnal; this being the very small area through which the very dense Bottom Water is descending at the rate $\mathcal{E}_{net}$ (because, assuming the abyssal ocean to be in a steady state implies that the sinking volume flux in this dense plume is equal to the net upwelling across the remainder of the surface), and we call this the first area at this height. The second area is the large approximately adiabatic interior area where the mixing activity is small. The third and fourth areas are the regions we have identified as the SML and BBL through which fluid sinks and rises respectively, in both cases caused by the divergence of bottom-intensified turbulent diapycnal buoyancy fluxes.

We now ask the question, in which of the last three regions would we expect there to be a linear vorticity balance that might support a horizontal circulation in the abyss in the sense of Stommel-Arons? The rather adiabatic interior region would be sufficiently linear as to obey the linear vorticity equation, but with very small diapycnal motion and almost horizontal density surfaces there is no appreciable vertical vortex stretching to drive a significant horizontal circulation. This leaves the BBL and the SML. The BBL contains much nonlinear dynamics and would not be a candidate for application of the linear vorticity balance. This leaves the SML where the linear vorticity balance might be thought to apply, especially as the vertical derivative of the diapycnal velocity in the SML is of the same sign as the Stommel & Arons vortex stretching; the difference being that in the SML the vertical velocity is negative and increasing in magnitude downwards! However, the realization following Callies and Ferrari (2018), that the adiabatic bolus advection is important in the SML in order to achieve the observed near-bottom stratification gives serious pause for concern, because in the context of the Eulerian average velocity, the effect of the bolus transport is equivalent to a large vertical viscosity which will likely render a linear vorticity balance unjustified. It seems then that we must conclude that with bottom-intensified diapycnal mixing there is no region in the abyssal ocean where the linear vorticity balance is appropriate except in the almost adiabatic interior which does not seem capable of driving an interesting circulation.

Callies (2018) has modeled the abyssal circulation using planetary geostrophic dynamics with Rayleigh friction, in a study with bottom intensified turbulence and sloping bottom topography. The strong and narrow upwelling in the BBLs on both the western and eastern sides of the bathtub basin was clearly evident. Unlike the Stommel-Arons case where the poleward flow is spread throughout

the zonal width of the basin and any equatorward flow occurs in the deep western boundary current, in their study poleward flow occurred near both western and eastern boundaries. Drake et al. (2020) have run this type of planetary geostrophic ocean model but now with strong bottom intensified mixing at a mid-ocean ridge, and with a realistic vertical stratification to which the model was restored in its southern-most region, as well as some runs with relaxation towards a constant vertical stratification. This study confirms that the BBL upwelling, and particularly the SML downwelling, are found to depend on the detailed nature of the topography and of the imposed vertical stratification. The meridional component of the horizontal circulation was concentrated in the regions of intense diapycnal mixing on the flanks of the mid-ocean ridge, with poleward flow on the eastern side of the ridge and equatorward flow on the western side of the ridge. These are regions in which the diapycnal mixing and the Rayleigh friction are both significant, and their horizontal circulation makes a striking contrast to that of the Stommel-Arons circulation.

3.8 Summary remarks

The realization, from microstructure observations, that much of the diapycnal mixing in the deep ocean is concentrated near the sea floor originally came from the Brazil Basin experiment more than twenty years ago. This bottom intensification of ocean mixing in the deep ocean has now been confirmed in many studies and in compilations of turbulence measurements (Waterhouse et al., 2014). Away from the rough topography at the ocean edges the background turbulent diffusivity is thought to be approximately 1×10^{-5} m^2 s^{-1}; a value which drives rather small diapycnal volume transports which are likely cancelled by the downwards diapycnal motion arising from cabbeling and thermobaricity.

With the early one-dimensional boundary layer theoretical studies of Garrett (1990, 1991) leading the way, we now have confidence that bottom intensified mixing leads to strong upwards diapycnal volume transport hard up against the sloping sea floor in what we now call the Bottom Boundary Layer (BBL). Immediately above this BBL, where the magnitude of the turbulent buoyancy flux decreases with height, is the Stratified Mixing Layer (SML) in which fluid parcels become denser and move through isopycnals towards denser (deeper) water. The Walin-type buoyancy budget approach yields rather simple relations between the diapycnal volume transports in the BBL and the SML as a function of how the net upwelling varies in the vertical as a function of buoyancy (Eqns. (29) and (30)). These relations indicate that the upwelling transport in the BBL is often several times as large as the net upward volume transport, and this has been confirmed in general circulation model studies. However, it must be said that to date, the diapycnal transport in the BBL has not been directly observed.

These observational and theoretical insights have direct implications for how we should parameterize diapycnal mixing in numerical ocean models, and also on the importance of a proper representation of bottom topography. If a diapycnal diffusivity is used to parameterize the small-scale turbulent mixing, then care should be taken to ensure that it varies sufficiently fast in the vertical so as to outweigh the increase in stratification in the vertical, thus ensuring that the magnitude of the turbulent buoyancy flux decreases with height. Note that this can only be checked after running the

model because the stratification changes during the model run. In addition, the ocean model needs to explicitly resolve or parameterize the sub-mesoscale instabilities that are thought to transport mass adiabatically along isopycnals when they slope significantly near ocean boundaries (Callies and Ferrari, 2018).

Several studies have shown that the net diapycnal upwelling transport in the abyss is a strongly increasing function of buoyancy (rather than being a fixed volume transport), and this has implications for the way that the dense plume-like sources of Bottom Water sink to the deepest parts of the ocean and then spread out at depth. The concept of continual entrainment into these plumes is due for wholesale revision.

Many studies have pointed to the importance of the topographic shape of the sea floor in regulating the upwelling of Bottom Water in the abyss, and this has been convincingly demonstrated by de Lavergne et al. (2017) where a variety of different mixing parameterizations all led to essentially the same net upwelling transport across isopycnals in the abyss.

While we have some understanding, based on buoyancy budget analyses, of the net diapycnal transport and the larger upwelling transport in the BBL, we do not yet have a clear view on the importance of these transports on the movement and diffusion of tracers in the ocean, nor of the dynamical consequences of these up- and downwelling motions in driving the horizontal abyssal circulation. The horizontal circulation patterns that can be seen in Callies (2018) and Drake et al. (2020) bear no resemblance to that of the Stommel-Arons circulation, and moreover, the bottom intensification of ocean mixing and the necessity of adiabatic bolus transport in order to achieve realistic vertical stratifications means that the linear vorticity balance on which the Stommel-Arons circulation rests is probably not applicable in any interesting part of the abyssal ocean. Since it is only a few years since the dominant paradigm has shifted from the horizontally uniform upwelling-diffusion balance of Munk (1966) to the paradigm of counter-flowing up- and downwelling transports near ocean boundaries, we can be hopeful that our understanding will develop rapidly in this area of oceanography.

4   Production Mechanisms for Boundary Mixing

The dynamics governing the physical evolution of stratified rotating flows over complex topography represent an especially difficult problem. A simple but key notion concerns the internal wave dispersion relation:

$$\vartheta = \sqrt{\frac{k^2 + l^2}{m^2}} = \sqrt{\frac{(\omega^2 - f^2)}{(N^2 - \omega^2)}} \tag{32}$$

for plane waves with wavenumber $\mathbf{k} = (k, l, m)$ and frequency ω. Wave frequency ω is simply related to the wave aspect ratio ϑ and very efficient coupling into small vertical scales occurs when this aspect ratio meets the topographic slope, $\alpha = \tan\theta$. In this section we present some of the basic turbulent mixing mechanisms, with an eye upon the one-dimensional model and its underpinning assumptions.

4.1   Internal wave reflection / internal tide generation

The prototype problem emphasizes conditions in which the large-scale inclination of the topography approximately matches that of ray trajectories associated with the energy-containing frequencies of the internal wavefield (Figure 8). Reflection and/or generation of internal waves under critical conditions for which wave aspect ratio ϑ (32) equals the topographic slope α are understood to result in significant velocity gradients and mixing (e.g. Eriksen, 1985; Garrett and Gilbert, 1988). Imprinted upon this class are the spatial inhomogeneity and temporal intermittency of the forcing parameters (i.e. tides, the background wavefield, topography). We note several caveats:
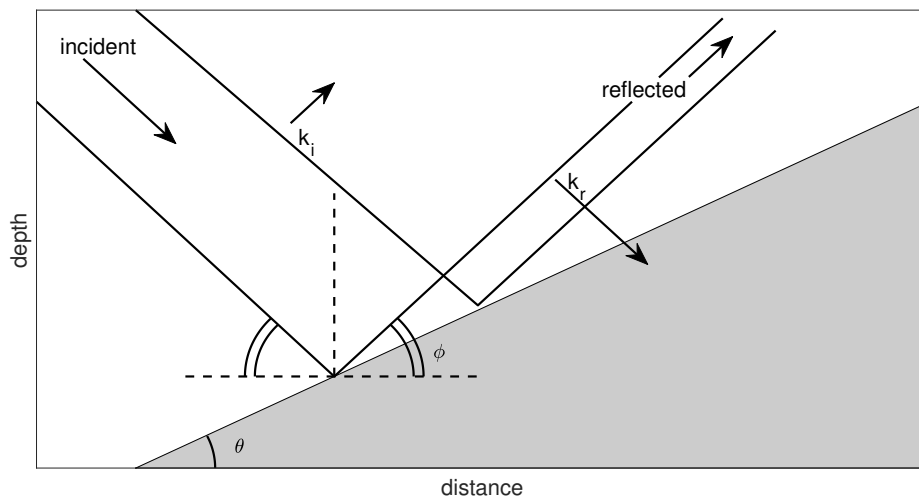

Figure 8: Ambient wave reflection. The key to understanding how the kinematic bottom boundary condition of no-normal flow changes the internal wave field over variable topography is contained in the internal wave dispersion relation. The internal wave frequency is determined not by wavelength, but rather by the angle of the wave vector, $\phi = \tan^{-1}(\sqrt{(k^2 + l^2)/m^2}$) (32), and this determines the trajectories of water parcels. A simple visualization can be achieved by drawing the crests and troughs of a wave incident at the boundary and requiring that the reflected wave matches the propagation of these crests and troughs along the boundary (black solid lines). Depicted are incident and reflected wavenumbers $\mathbf{k}_i$ and $\mathbf{k}_r$ with phase propagating in the direction of the wavevectors. Wave frequency, and hence ϕ, are preserved under reflection, independent of the orientation of the slope α. Transformation of incident energy to very high wavenumber $\mathbf{k}_r$ occurs at a frequency for which $\phi \cong \theta$ (and thus $\vartheta \cong \alpha$), leading to enhanced wave-breaking and mixing (e.g. Chalamalla et al., 2013). Figure from Bracco et al. (2020), after Garrett (1991).

- Internal wave reflection is a less productive mixer than the idealized semi-infinite problem might have you believe. The wave reflection process was the target of a process study (Eriksen, 1998) on the steeply sloping flanks of Fieberling Guyot, a tall seamount in the eastern Pacific. While turbulent dissipation was significantly enhanced toward the bottom (Toole et al., 1997), the vertical shear responsible for that dissipation was enhanced in the along-slope direction, rather inconsistent with the linear internal wave kinematics that underlies figure 8. The reason is
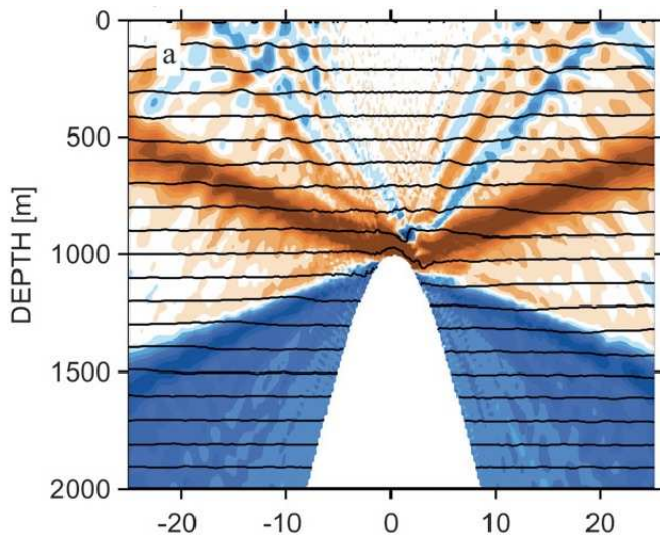
Figure 9: Internal tide generation for a super-critical ridge, in which internal waves of the tidal frequency have smaller aspect ratio (32) than the topographic slope α. The baroclinic velocity field from a model simulation by Klymak et al. (2010) is depicted. There are 4 main beams emanating from the ridge crest associated with the forcing and super harmonics at greater angle to the horizontal.

unresolved. However, there are ridges and ravines running up and down the flanks of the Guyot like that depicted in figure 10 that could give rise to the along-slope shear. One finds that the linear reflection problem does not have a solution for super-critical incident waves *if* the bottom boundary condition (4b) requires the reflected wave to have an along-slope component (Eriksen, 1982). More speculatively, unlike the semi-infinite plane, the ocean does have a free surface.

• There are similar issues with internal tide generation. The kinematic bottom boundary condition (4b) stating that flow parallels the bottom is nominally applied at bottom, $z = h(x, y)$. In a small amplitude limit, for which $\vartheta \gg \alpha$, one approximates this by applying (4b) at $z = 0$. The benefit of this approximation is that one can take Fourier transforms of the topographic roughness fields in figure 3 and, in a simple manner, translate those transforms into the internal wave response and ultimately to turbulent dissipation associated with wave breaking (Polzin, 2004b). The draw-back is that one loses connection with the enhanced shear and non-linear phenomena implied by the contraction of ray tubes in figure 8.

Expectations of a strong enhancement of vertical shear associated with the contraction of ray-tubes are not supported by observations from the Brazil Basin (Polzin, 2004b). The manner in which this was inferred is that a Fourier representation of topographic roughness was routed through a linear model of internal tide generation and this served as the boundary condition for a nonlinear internal wave propagation model that, in turn, provided an estimate of turbulent dissipation as a function of height above boundary. The essence of that nonlinear propagation model was a direct relationship between internal wave shear and dissipation (Polzin, 2004a). Both predicted shear and predicted dissipation using the small amplitude topography approximation were in agreement with observations. Qualitative assessments (Polzin, 2004b, see their appendix) using a finite topography model (Baines, 1973) suggested an order of magnitude enhancement of shear variance associated with near critical topographic slopes that was not observed.

31

The following rationale was put forward concerning why the mathematically more sophisticated theoretical treatment was not consistent with the observations: that theoretical treatment of finite amplitude topography is essentially one-dimensional. This one-dimensional assumption may be germane to a continental slope - shelf break - continental shelf planform or an extended feature such as the Hawaiian Ocean Ridge, but the abyssal hill roughness situated atop the Mid-Atlantic Ridge in figure 3 is two-dimensional. In one-dimension, the flow is forced to be up and over topography. In two dimensions there is the potential for steady flow to go around an obstacle in instances in which it might otherwise be 'blocked' from going up and over (e.g. Epifanio and Durran, 2001).

In summary, basic linear internal wave kinematics points to near critical slopes for which $\vartheta \cong \alpha$ as being places that should host enhanced internal wave shear and mixing. However, when one gets to the point of being quantitative, there are some essential details about steep, rough topography that we do not understand. In particular, these inconsistencies point to expectations based upon idealized one-dimensional representations as being naive.

Idealized simulations of critical and near-critically reflected internal waves / internal tide generation (Slinn and Riley, 1998; Gayen and Sarkar, 2010; Chalamalla et al., 2013; Sarkar and Scotti, 2017) reveal episodic convective near-boundary overturning associated with the kinematics of the internal waves. The picture is one of the wave tripping over itself in an 'internal swash zone'. The efficiency of convective mixing near the boundary rather argues against a generic length scale suppression of Γ to support a mid-depth minimum in buoyancy flux. Significant ($O(1)$) perturbations of density gradients that cycle with the wave period are inconsistent with with the underpinnings of a mixing length closure (2) and suggest skepticism.

The Supercritical Limit

The supercritical ($\vartheta \ll \alpha$) limit of the internal tide generation problem (figure 9) is one that can also host strong mixing. Here, the topography is sufficiently steep that the contraction of ray-tubes plays little role in enhanced shear to drive mixing. Rather, enhanced near boundary mixing is associated with a downslope jet and overturning wave in the lee of the ridge. These features are reminiscent of the internal hydraulic response to a steady flow, figure 11. Here, however, the downslope jet and overturning wave cycle from one side of the ridge crest to the other in sync with the barotropic tidal flow. The foundations of a mixing length theory, i.e. small perturbations on a steady flow, are likely challenged in this environment.

4.2   Sub-inertial Flow and Topography

Rough Topography on a Slope

A second class of turbulence forcing mechanisms emphasizes subinertial flows (i.e. eddies and mean flows) in combination with topographic variability. When the amplitude of the topographic variability is small and has length scales permitting the radiation of internal waves, then internal lee waves (Bretherton, 1969; Thorpe, 1992) are generated (Figure 10). When the topographic variability is large, however, near-boundary wave breaking, hydraulic like effects, flow separation and vortex shedding arise, and dominate the radiating response, e.g. Baines (1997); Figure 11. Boundary

mixing associated with these finite amplitude phenomena can be quite intense and typically occurs in stratified waters apart from the boundary.
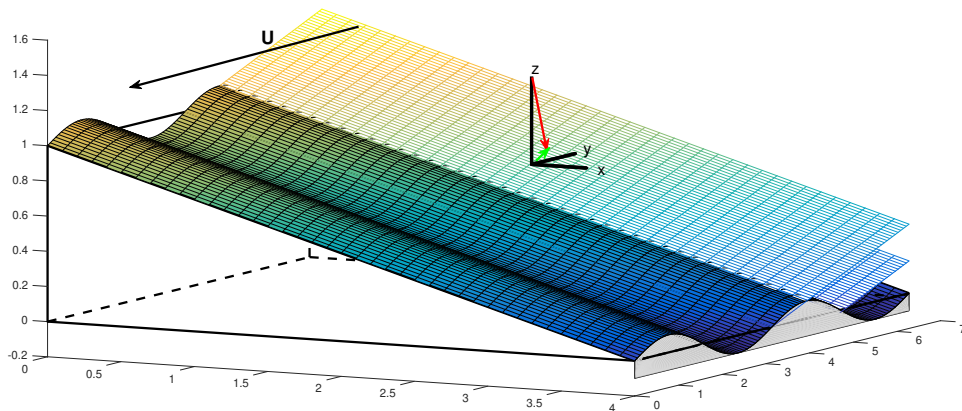

Figure 10: Lee waves: Mean flow over irregular topography can induce radiating internal waves if the topographic irregularities superimposed on the slope have a 'small' amplitude (figure from Bracco et al. (2020), after Thorpe (1992)). In this case one assumes a quasi-stationary internal wave response that varies on the time scale of the background flow. Mean flow direction is indicated by the arrow in association with U. A right-hand x - y - z coordinate system defines the orientation of the wave vector (red) normal to the wave phase planes. On an inclined plane the projection of the wavevector onto the horizontal (green) lies in the upslope direction. Without the inclined plane, the dynamical transition between waves and hydraulics occurs when the topographic perturbations have an amplitude similar to that of the lee wave, flow blocking initiates and vertical shear in the wave response is approximately equal to the buoyancy frequency N. The dynamical impact of the inclined plane as concerns blocking/splitting is largely unexplored.

There is a wealth of knowledge within the atmospheric science community concerning stratified flows over topography. Such studies are usually performed for isolated topography (with length scale ℓ) in a non-rotating limit, specifically $U/f\ell \gg 1$, where U is the typical lateral flow velocity and f the Coriolis parameter. Assuming vertically uniform background flow and constant stratification, over one-dimensional topography with height h and length ℓ scales, the steepness parameter $Nh/U : 1$ separates a linear wave regime from a high drag state featuring hydraulic effects. In two dimensions this boundary is somewhat smaller, $Nh/U : 1/2$ (Nikurashin et al., 2014), with the transition between 1-D and 2-D requiring elongated ridges of length-to-width aspect ratios of 1:10 (Epifanio and Durran, 2001). One can argue for this dynamical boundary on the basis of energetics: flow below the topographic crests lacks sufficient kinetic energy to trade for potential energy to traverse the ridge crest and is either blocked, or in 2-D, splits and flows around the topographic obstacle. The second way to argue for this Nh/U parameter boundary uses linear wave kinematics: assuming a steady response, the stationary lee wave has an apparent frequency of kU with horizontal wavenumber $k = 1/\ell$, a vertical wavelength of U/N, and propagates at a slope with respect to the horizontal of k/m that must exceed the topographic slope h/ℓ in order for the linear response to be valid.
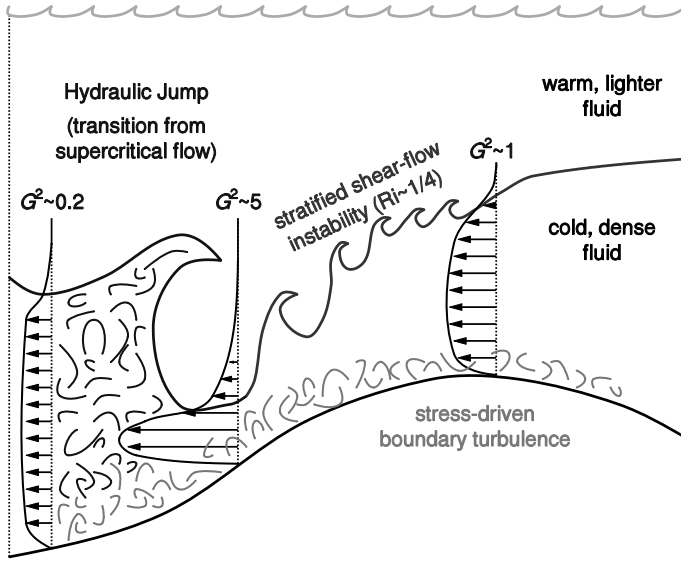
Figure 11: Internal hydraulics: Intense mixing can occur if the topographic irregularities are 'finite amplitude' and a parameter regime of internal hydraulics is entered (figure from Nash and Moum (2001)). Turbulence and mixing occur in conjunction with bottom stress in an accelerating downslope jet, high shear on an interface with overlying fluid and within the hydraulic transition (jump).

Extrapolating from the atmospheric literature is hazardous for the following reasons:

- The oceanic paradigm is one in which topography is not isolated and the scales of topography are such that rotation cannot be neglected $[U/f\ell \sim O(1)]$; with rotation, the linear kinematics that links wave steepness to energetics are fundamentally altered.

- The presence of a large-scale slope alters the kinematics of the linear problem so that the lowest frequency internal wave has a wavenumber that points upslope (Thorpe, 1992); see Figure 10) rather than being parallel to the roughness wavenumber. This fundamental change in the steady linear solution modifies the blocking criteria in uncertain ways.

- Filtering of topography to address lee wave generation (Scott et al., 2011; Nikurashin and Ferrari, 2011; Kunze and Lien, 2019) is problematic because the bottom boundary condition that flow has to be parallel to the boundary (4b) is nonlinear in topographic height. Claims (Kunze and Lien, 2019) that filtered topography typically lands in a small Nh/U parameter regime seem to miss the point: a simple filtering of the topography is implicitly equivalent to a linearization and the bulk of the topographic height variance lies in the subinertial $[U/f\ell < O(1)]$ regime. Figure 10 presents an idealized representation of multi-scale topography in which the linear wave generation problem is understood to differ. The dynamical impact of the inclined plane on flow blocking is largely unexplored.

Global estimates of lee wave transformation rates (Scott et al., 2011; Nikurashin and Ferrari, 2011) have value in that they provide order of magnitude constraints on the process. They depend upon a hypothesis of a quasi-stationary response, either lee-wave or hydraulic, to quasi-stationary flow. Verification of this is difficult. Moored ADCPs embedded in current meter arrays about a large scale $[U/f\ell < O(1)]$ seamount in Drake Passage (Brearley et al., 2013; Cusack et al., 2020) and along a smaller scale $[U/f\ell > O(1)]$ ridge on the western boundary off the Bahamas (Clément

et al., 2016; Evans et al., 2020) document that the vertical shear variance is modulated on eddy time scales but find this enhanced vertical shear appears at near- and super-inertial Eulerian frequencies rather than being a quasi-stationary lee wave response. Whether this time dependence relates to the forcing of super harmonics in a wave problem (Nikurashin and Ferrari, 2010) or relates to transients apparent in models of the boundary layer on a sloping bottom (section 4.3) are open questions.

Constrictions, Gaps and Passages

One perspective concerning the global upwelling of abyssal waters is an abrupt departure from the conical basin pictured as a prototype of hypsometric issues in section 3. This perspective considers the abyssal circulation as a series of interconnected basins. These basins are related through topographic constrictions, gaps and passages featuring enhanced mean flows and intense mixing related to hydraulic phenomena with the pressure head for that flow set up by external mixing processes (tides, etc.) in the interior basin. The importance of mixing related to hydraulic processes is made manifest in major passages by abrupt spatial changes in bottom potential temperature (e.g. Mercier and Morin, 1997; Alford et al., 2013).

The Deep Basin Experiment (Morris et al., 2001) was a multi-national effort to quantify the input and output of dense water from the Brazil Basin, relating to control volume studies in the early 1980-s (Hogg et al., 1982; Whitehead Jr and Worthington, 1982). From these early studies, CTD transects across the southern entrance to the basin revealed near-vertical isopycnals banked upon the eastern side of the channel. This was interpreted by Hogg (1983) as a product of rotating hydraulic withdrawal in the face of slowly varying topography, with those steep isopycnal slopes geostrophically balanced rather than implying much about mixing. In the following Deep Basin Experiment the northeastern exit represented by the Romanche and Chain Fracture Zones was surveyed with fine and microstructure instrumentation (Polzin et al., 1996). Even though this exit is extensive, the passages are at low latitudes (within one degree of the equator) such that intense mixing associated with hydraulically controlled flows and internal hydraulic transitions was identified as being responsible for a 0.41 °C increase in bottom potential temperature.

With reference to figure 11, mixing in an internal hydraulic scheme can occur in conjunction with intense shear on an interface and subsequent hydraulic transitions (jumps) or in conjunction with bottom drag in a downslope jet. In the Romanche Fracture zone the intense shear occurred on the (relatively) strongly stratified boundary between North Atlantic Deep Water and Antarctic Bottom Water and the relative maximum of dissipation there implied a downwelling of Deep Water and upwelling of Bottom Water. The control volume estimates of Mercier and Speer (1998) and turbulence estimates in Polzin et al. (1996) provided fodder for a back-of-the-envelope estimate presented in Ferron et al. (1998) which suggested that, despite the hydraulic processes leading to mean dissipation rates orders of magnitude larger than those associated with tidal mixing above roughness in the Brazil Basin (Polzin et al., 1997), both external tidal and local hydraulic processes were required to explain the control volume constraints for mass and buoyancy (upwelling and mixing).

The robustness of that result and the spatial separation between localized hydraulic processes within the Romanche vs tidal mixing in the eastern Atlantic provides the following insight. The hydraulic flow is associated with a pressure head between the western and eastern equatorial Atlantic:

the densest water is in the west. The reason for that pressure head is the broadly distributed mixing in the farfield: without complete mixing of buoyancy by hydraulic processes, in the absence of a far-field (tidal) mixing process, dense water will slowly fill up the interior basin and diminish the pressure head. Thus, such hydraulic transitions are not going to be the rate controlling process for abyssal upwelling.

Alford et al. (2013) present a similar example of intense mixing associated with hydraulically controlled flows within the Samoan Passage. The Samoan Passage is a 40 km wide notch in the South Pacific bathymetry through which flows most of the water supplying the North Pacific abyssal circulation. Similar to the Romanche Fracture Zone, it is relatively low latitude (8° S) and the issue of hydraulic control appears in conjunction with the smaller scale topographic features within the Passage rather than the broader scale topography. These locations constitute 'hot spots' of mixing that dominate the Passage average (Voet et al., 2015). Cusack et al. (2019) argue that hydraulic processes in a supercritical flow regime in the hot spots dominate over tidally induced mixing processes and are very persistent in time. Application of an analytic model for internal hydraulic jumps in a stratified flow (Thorpe et al., 2018) revealed a remarkable ability to predict jump locations, changes in the baroclinic structure of the flow and turbulent dissipation. The model has a continuously stratified interface between two homogeneous layers. Transitions involving this interface were identified and could provide a rationale for upwelling and downstream warming trends of bottom potential temperature without directly invoking the one-dimensional model or its boundary layer physics.

MacKinnon et al. (2008) describe observations from the Atlantis II Fracture Zone, which presents a pathway for Antarctic Bottom Water and Circumpolar Deep Water from the abyssal Southern Ocean into the deep Indian Ocean. Enhanced mixing along the center line of the Fracture Zone was hypothesized to be associated with the interaction of internal waves, possibly of tidal origin, with the vertical shear of an $O(0.2 \text{ m s}^{-1})$ mean current. The along channel evolution of watermass properties suggested greater diapycnal transformations than documented by the center line measurements. The issue of mixing associated with internal hydraulics was discounted. The measurements do not appear to speak to the potential of mixing along the sloping sidewalls of the Fracture zone.

A microcosm of these concerns exists within rift valleys and smaller fracture zones. Within the Brazil Basin, a proposal (Thurnherr et al., 2005) that basin wide mixing was largely sustained by mean flows in conjunction with occasional sills cutting across fracture zones and internal waves interacting with these mean flows (Clément and Thurnherr, 2018) seems not to have carried the day (Thurnherr et al., 2020). The circuitous route to this conclusion seems to originate in geographic groupings of microstructure profiles into valley, slope and crest bins (St. Laurent et al., 2001) that are visually inconsistent with data presented in figure 3 of Polzin et al. (1997). What is called for are dynamically grounded models (Polzin, 2004b, 2009; Thorpe et al., 2018) to aid understanding of the vertical structure and patterns of dissipation profiles, rather than geographic groupings unrelated to the underlying physics. From this dynamical perspective the singular role of this fracture zone valley is that it acts as a conduit for mass transport, pursued further in section 5. Different conclusions might be applicable to the rift valleys (Thurnherr, 2006; St Laurent and Thurnherr, 2007; Tippenhauer et al., 2015) of slow spreading ridges, such as the Mid-Atlantic Ridge, in which the rift

valley side-walls are significantly steeper than adjacent abyssal hills and the interesting internal tide generation physics occur at the topographic crests, e.g. figure 9.

4.3   Friction and Sub-inertial Flows

A third class of forcing mechanisms is provided by turbulent stresses associated with drag at the bottom boundary (equation (4a)) and an insulating condition on temperature (buoyancy, equation (4c)). Over sloping topography the drag triggers cross-slope mass and buoyancy transport (Figure 12), ultimately leading to a reduction in the near-bottom flow and a decrease in drag as the near-boundary buoyancy anomalies come into geostrophic balance. The steady-state limit, with zero bottom velocity, is known as the arrested Ekman layer (Garrett et al., 1993). In the case in which the flow is oriented in the direction of Kelvin wave propagation, Ekman transports are downslope, near-boundary stratification is reduced and the situation is referred to as a downwelling Ekman layer. For retrograde motion, upslope transport leads to increased stratification at the boundary. Below we focus upon the downwelling case and avoid the arrested state.
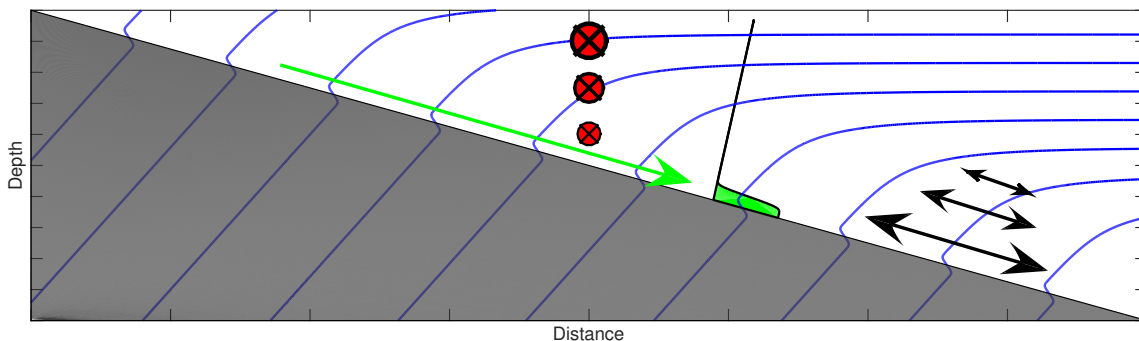

Figure 12: Mean flows and friction. This schematic depicts an Ekman layer over a sloping boundary in its downwelling configuration, rendered for a southern hemisphere. Drag exerted on the along-slope flow (red bullets and crosses) results in a downslope Ekman transport (green arrow and green near-boundary profile), advecting light water downslope and tilting isopycnals (blue contours). Statically unstable conditions are attained, driving boundary layer turbulence similar to that of a convectively unstable atmosphere. Note that the isopycnals are not normal to the bottom on the scale of the figure. The system has a resonance at frequencies for which $\vartheta = \alpha$ and the boundary forcing is carried aloft by mechanisms related to these cross-slope motions, depicted as black arrows. The schematic depicts the convectively unstable region having a smaller height scale than the penetration depth of the turbulent momentum flux (bottom drag), which in turn has a smaller height scale than the cross-slope process.

There are two key points. First, this downwelling boundary layer system is driven by downslope transports of light water which results in statically unstable conditions on a height scale determined by the penetration of the turbulent momentum flux into the fluid. This places the oceanic boundary layer into a convectively unstable parameter regime, similar to the daytime atmospheric boundary when heated from below (Stull, 2012). Second, this convective process can resonantly couple with

internal wave band motions for which $\vartheta = \alpha$, figure 13.
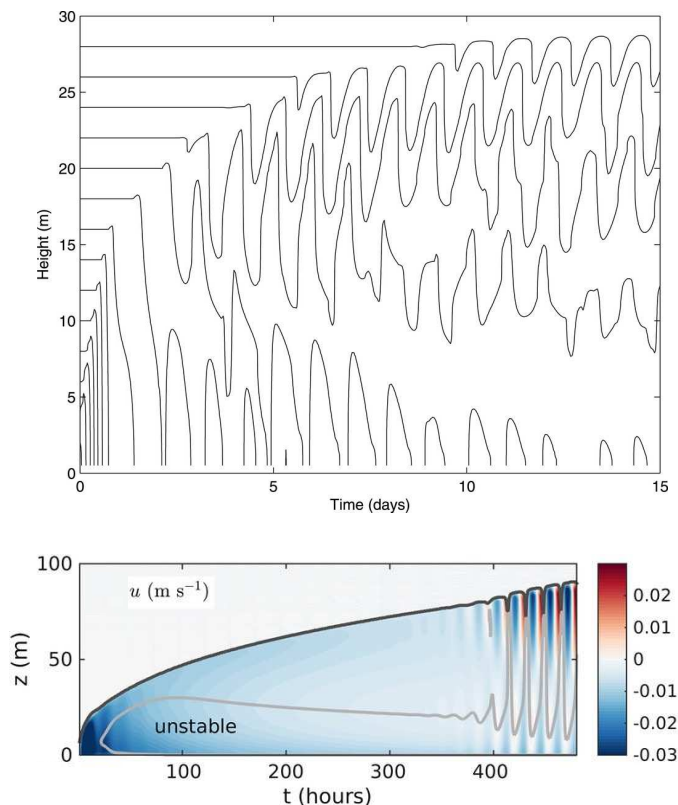

Figure 13: A key issue for the Ekman layer process is the limited penetration depth of the turbulent drag relative to the arrest height scale for typical abyssal stratifications. In the one-dimensional models of the sloping Ekman layer, mixing is carried aloft by the agency of cross-slope motions at the resonance frequency, for which $\vartheta = \alpha$. The upper panel depicts isopycnal contours from Brink and Lentz (2010) for an $s \sim O(1)$ simulation and the lower panel depicts the cross-slope velocity from Umlauf et al. (2015) at a somewhat smaller Burger number ($s = 0.22$). The onset of cross-slope motions is much delayed in the lower Burger number simulations.

Using a Large Eddy Simulation (LES) of the downwelling Ekman layer, Ruan et al. (2019) point out that their model behavior parallels that of the prototypical 'night-time' atmospheric boundary layer in which the surface is cooler than the overlying air, in which the boundary provides a source for buoyancy and provides for stratification. Taken at face value, this is bizarre: the downwelling Ekman layer exhibits convection which is the prototypical *daytime* atmospheric boundary layer when solar insolation results in a surface that is warmer than the air above. A potential reconciliation is to note that the insulating bottom boundary condition requires positive stratification and the question becomes, 'what is the length scale over which this pertains?'.

In the LES model there are two modes of behavior. If frictional effects are large, the boundary layer is turbulent. If buoyancy forcing is large, the boundary layer 'laminarises', i.e. it becomes non-turbulent. In the atmospheric boundary layer, the metric to judge whether friction or buoyancy forcing is 'large' lies in the size of the Obukov length scale relative to about 100 wall units (Stull, 2012). If the Obukov length scale is greater than approximately 100 wall units, the boundary layer is turbulent. Ruan et al. (2019) find that the downwelling Ekman layer exhibits a similar transition when the buoyancy forcing is expressed as the depth integrated downslope Ekman buoyancy

transport.

Within a molecular sublayer the flux-gradient relation (2) holds and within this molecular sublayer the insulating bottom boundary condition (4)c provides $\partial_{\hat{z}}b = 0$. This translates into positive stratification at the boundary, $\partial_z b > 0$. The question apparently becomes, 'when is the flow strong enough that this molecular condition can't project into/past the viscous sublayer and trigger a laminarisation of the boundary layer?' The answer, from Ruan et al. (2019), is that their modified Obukov length scale needs to exceed roughly 100 wall units in order for the flow to laminarize. Whether such a transition exists for a hydrodynamically rough surface, one in which surface texture (e.g. gravel) extends into the viscous sublayer, is an open question, but the important point here is that the discussion concerning the structure of the 'BBL' and 'SML' has been moved from a $\hat{z}$ of approximately 100 meters (Ferrari et al., 2016) to a $\hat{z}$ of 1 centimeter.

Observations that document the essential convective physics are rare, with prominent exceptions presented in Moum et al. (2004) and Kolås and Fer (2018). Many additional studies of observational inference (Trowbridge and Lentz (2018) and references therein) similarly come from shelf and upper slope regions. Our understanding of the downwelling Ekman boundary layer in the deep ocean is thus grounded in idealized modeling studies executed in the slope-rotated coordinate system (6). The most relevant of these implement turbulent closure schemes underpinned by the concept of an unstratified wall layer or the resulting quadratic drag (4a).

The salient features of these modelling studies are, first, that the slope Burger number $N\sin\theta/f$ (equation (8)) is arguably the key nondimensional parameter determining the structure and long time evolution of the boundary layer. The effects of gravity relative to rotation ensconced in N/f is a close second, and, apart from the near bottom region, the bulk of the boundary layer is stratified with a height scale proportional to U/N. Two figures serve to illustrate our points. The first example is from Brink and Lentz (2010) with $(s, N/f, U/N) = (0.98, 195, 20.5m)$ in which time dependent cross-slope oscillations at the resonant frequency $\omega(\alpha)$ rapidly set in. The second example is from Umlauf et al. (2015) with $(s, N/f, U/N) = (0.22, 44.7, 44.7m)$ in which the onset of cross-slope oscillations is relatively delayed.

The cross-slope variability is crucial but our current understanding of that variability is limited. In one-dimension the cross-slope variability is forced to map onto internal wave kinematics. In two dimensions it is understood (Allen and Newberger, 1998) that the arrested state of the 1-d model is unstable to symmetric instabilities if the Ertel potential vorticity has the opposite sign from its interior value. Ruan et al. (2019) argue from 3-d Large Eddy Simulations that the oscillatory motions are triggered by an episodic molecular laminarization within the log-layer prior to the onset of arrest. Regardless of the physics, the cross-slope variability serves to ventilate the boundary layer at heights greater than the turbulent drag is able to penetrate, further bending isopycnals toward the bottom and, through the agency of thermal wind, diminishing the bottom velocity to the arrested state.

However limited our understanding may be, there is a *clear* association of fine- and microstructure vis-a-vis rough steep topography and subinertial near-bottom velocity, Naveira Garabato et al. (2004). The potential relevance of bottom friction to such measurements is provided by dedicated observations about a relatively nondescript seamount in Drake Passage, in which the internal waveband shear variance is modulated in response to the subinertial flow (Brearley et al., 2013) and that

modulated internal wave variability does not agree with linear internal wave kinematics (Cusack et al., 2020). With environmental parameters of $U = 0.1$ m s^{-1} and $N = 1 \times 10^{-3}$ s^{-1}, that non-descript hill (c.f. figure 1) maps onto $(s, N/f, U/N) = (0.6, 10, 100\text{m})$ and has an advective time scale ($f/kU \cong 0.3$) that is too large to efficiently generate quasi-stationary lee waves. Yet that time scale is large enough to consider the initiation of boundary layer coupling with cross-slope motions without being so large that the arrest stage is of concern.

This boundary layer process is more clearly, yet imperfectly, seen in measurements from an abyssal passageway. Naveira Garabato et al. (2019) present preliminary results from a process study documenting the mixing and transformation of newly formed Antarctic Bottom Water as it transits one of the major pathways by which Anarctic Bottom Water is exported into the World Ocean. They document intense mixing of weakly stratified ($N/f \sim 5$) water over steep complex topography ($s \sim O(1)$) in which bottom enhanced turbulence extends multiples of $U/N \sim 400$ m above the bottom. They interpret their measurements in terms of submesoscale instabilities resulting from a sign reversal in Ertel potential vorticity. Microstructure data reported in Spingys et al. (submitted) document a highly efficient mixing process with $O(1)$ dissipation ratios Γ_μ (18).

Finally, as concerns the Ferrari et al. (2016) proposal that the one-dimensional model be characterized by a mid-depth minimum in the buoyancy flux, the essential physics in the downwelling Ekman layer concerns convection and convection is understood to host an efficient dissipation ratio (section 2.5.2, Gregg et al. (2018)) that is essentially nonlocal and not captured by a mixing length closure.

5 Discussion

We began this review by invoking the starting lines from many a fairy tale. A well honed fairy tale is not necessarily complete fiction, often there is allegorical truth. That preamble contrasts with the more serious tone of scientific writing, in which the epistemology of science is empirical ratification. Upon this point, what we have confidence in, is rather meager. There is a dire need for observations to constrain the problem and theoretical efforts would benefit from turbulence modeling to address the myriad of assumptions and approximations.

The key piece that underpins our understanding of upwelling is the diapycnal advection-diffusion balance (9), which makes direct reference to the divergence of the density flux. Direct estimates of this flux are quite difficult, so what we have done is to cobble together bits and pieces from our knowledge of turbulence and idealized models (section 2.5.2, 3 etc.). Turbulence modeling studies will fundamentally improve our understanding and constrain the uncertainty. There is an associated question of representing boundary mixing in state of the art regional simulations (e.g. Bracco et al., 2020) that will similarly require significant effort.

Substantial progress could be achieved with direct estimates of density and momentum fluxes, and in particular in conjunction with the spatial distribution of time varying form drag. We require an extension of bottom lander estimates (Shaw et al., 2001) in the vertical (to $\hat{z} > U/N$) in steeply sloping ($s \sim O(1)$) environments and internal wave band estimates (van Haren et al., 1994; Gemmrich and van Haren, 2002) into turbulent frequency bands. Having a direct estimate of bed stress resulting

from turbulence (Perlin et al., 2005) and estimates of reduced mixing efficiency with decreasing height above the boundary (Holleman et al., 2016) present technical issues, but our ignorance largely lies within the internal wave and submesoscale frequency bands, and centers upon the questions of how system resonance and rotation alter the behavior of the system. These frequencies and questions could be tackled with focused numerical modelling efforts, clarifying the possible coupling between friction and form drag. Important phenomena will arise in 3-dimensions relating to nonpropagating form drag and these will be difficult to address numerically.

We do understand that there is an association between mixing and steep rough topography. The parameters in play are fairly clear: a non-dimensionalized topographic slope, especially in relation to the critical slope of internal wave dynamics for which $\vartheta = \alpha$, external forcing about that resonance, a metric of stratification relative to rotation N/f and the height scale U/N, in which U/N appears in many physical contexts. Disentangling the effects of nonpropagating form drag from boundary layer physics over sloping topography will require significant effort. A coordinated survey of this extended parameter space would be a significant community undertaking, but would amount to more than incremental progress.

Beyond that broad summary, we close by trying to frame open questions with the hope of clarifying pathways to progress. Unsurprisingly this amounts to a dance around putting an observation into a numerical or theoretical construct.

Open Question #1: Representing Rough Topography

The first, and foremost, question relates to figure 3, in which the strongly enhanced mixing over the MAR is supported by rough and steep topography. All these glorious mountains are bulldozed in the construction of a General Circulation Model (GCM), which may even lack a coarse representation of the fracture zone valleys that serve as conduits of mass transport to the MAR crest (Thurnherr et al., 2005)). Figures 14, 15 and 16 attempt to depict the physical situation. Figure 14 is a 3-d representation of multibeam bathymetry along a fracture zone valley with up-valley flow from west to east. Downwelling across isopycnals is depicted above the topography in association with an increase in dissipation toward the bottom, *upwelling* is depicted as fluid peels off from the valley axis and enters the area between the abyssal hills. The rationale for this is a hypsometric argument contained in figure 15: denser isopycnals occupy less surface area and thus the area integrated diapycnal fluxes are smaller. The upwelling profile in figure 15 (Polzin, 2009) was estimated as

$$\epsilon(Z) = \int_0^\infty \epsilon(z) P(z \mid Z) dz \tag{33}$$

in which $\epsilon(z)$ is a parameterized estimate of the observed profiles and is monotonically increasing in z over the bottom most 1500 m. The factor $P(z \mid Z)$ represents the probability density of having a station height z given the model coordinate (depth) Z. The vertical component of the diapycnal velocity w^* then follows as (McDougall, 1989):

$$w^* N^2 = \frac{\partial \, \Gamma \epsilon}{\partial Z} \, , \tag{34}$$

in which the mixing metric Γ was assumed to be 0.2. In this calculation the abyssal hill topography was assumed to follow a Gaussian distribution with a root-mean-squared height of 110 m based upon a parametric spectral characterization of abyssal hills (see Polzin (2009) for details). The underlying dissipation curve $\epsilon(z)$ was prescribed as the dynamically motivated characterization presented in Polzin (2004b). The resulting diapycnal velocity supports a pattern of upwelling and downwelling reminiscent of Ferrari et al. (2016), section 3: the net represents upwelling and is a small residual of contributions above and below the mean depth. This result has been attained *without* invoking *ad hoc* arguments about the near-boundary structure of the buoyancy flux, *a la* Ferrari et al. (2016). The relevance of abyssal hills to this conversation can alternately be posed as in Ferrari et al. (2016) by reducing the hypsometric arguments concerning surface area in (11) to the length of the boundary in a line integral. While what one wants in that representation is the length of the line along a grounding isopycnal, contours of constant depth using multibeam data, figure 16, are highly convoluted and the inferred line lengths are more than an order of magnitude greater than the meridional extent of the figure. The abyssal hills are consistent with a fractal process (Goff and Jordan, 1988), which in this context means that as one increases the effective resolution of the underlying topographic data set, the contour length increases without bound (e.g. Mandelbrot and Mandelbrot, 1982). Figures 14-16 provide a strong argument that the locus for the rate controlling dynamics of abyssal upwelling reside in the abyssal hills. With that statement, though, comes a question. How does one properly represent the boundary conditions (equations (4)) in a GCM when such radical changes have been made to the bottom boundary?

How much cause for concern is there in bulldozing the mountains to create the gently sloping topography of a GCM? Take the example of the Brazil Basin and say that one eliminates the abyssal hills to create this flat landscape, and by implication the upwelling relating to their hypsometric variability in figure 15. One is left with offset fractures (valleys) that transport dense water to the ridge crest, cut by occasional sills (Thurnherr et al., 2005). If one represents the mixing associated with the abyssal hills using $\epsilon(z)$ without (33), the in-cropping of isopycnals into the valleys creates its own hypsometric variability and upwelling results (Thurnherr et al., 2020). However, these valleys are also eliminated in the creation of the flat landscape of a climate GCM (figures 14 & 16). A message from the study of de Lavergne et al. (2017) is that, if one has a reasonable representation of the overall *energetics* within a basin interior, changing the spatial distribution of mixing within the GCM will produce a consistent representation of globally averaged upwelling that reflects global hypsometry.

The consequences of not acknowledging that the abyssal hills have been bull-dozed are at least two fold. First, one is put in a position of invoking vertical structure in the buoyancy flux (Ferrari et al., 2016) in order to promote upwelling, and in so doing inviting commentary about the lack of physics underpinning that assertion. Second, weakly stratified water will tend to accumulate near the boundaries and one is put in a position of invoking a tertiary process such a baroclinic instability to ventilate the boundary. In Callies (2018), submesoscale eddies of similar scale and aspect ratio of abyssal hills are proposed to address the ventilation of the bottom boundary, a need that is arguably a result of the creation of the flat landscape in a GCM. We remind the reader of a similar conversation involving figures 1 & 2 detailed in the Introduction.

One perspective in which such details matter is the context climate change predictions. Global ocean upwelling underpins the millennial time scale of climate trends and one can view such trends as small imbalances in budgets that reflect the detailed differences discussed herein. In this context, a goal should be for GCMs to acknowledge the underlying physics.
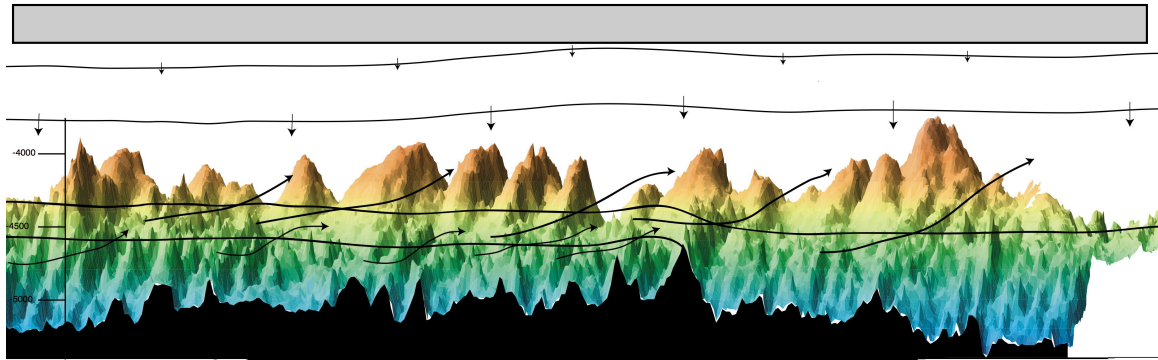

Figure 14: A schematic depiction of the secondary circulation proposed in Polzin (2009) along the axis of a fracture zone leading from abyssal plain to ridge crest. Lines without arrows represent isopycnals. Lines with arrows represent particle trajectories with net upwelling across isopycnals. Upwelling in this schematic is associated with the near boundary decay of the internal tide generated/scattered in association with abyssal hills atop the ridge, along with hypsometric arguments. The black foreground is the bathymetry profile along the canyon axis. The peaks atop the ridge are abyssal hills. The canyon axis is significantly smoother than the adjacent ridge, but is occasionally cut by abyssal hills extending from the ridge. These features form sills that block deep flow up the canyon axis. The light grey shading depicts the face of a medium resolution GCM grid cell, $3/4° \times 3/4° \times 250$ m.

Open Question #2a: sSpecification of Mixing Efficiency and its Near-Boundary Structure

Within this GCM world, one can ask how to configure the model to support upwelling. Two direct answers have appeared. One approach (de Lavergne et al., 2016b) relies upon a characterization of direct numerical simulations of turbulence that contend the mixing efficiency decreases to small values as turbulent intensity quantified by R_{eb} (20) increases beyond a value of 400 (Shih et al., 2005) and play off weakened abyssal stratification to attain upwelling. Recent assessments of microstructure (Ijichi et al., 2020; Spingys et al., 2001-in press) in this high R_{eb}, low N parameter regime have demonstrated that mixing efficiency estimates do not support a general decrease in Γ_μ with increasing R_{eb} for intense turbulence. A second approach assumes a well-mixed BBL in which the vertical buoyancy flux diminishes linearly to zero as the sea floor is approached (McDougall and Ferrari, 2017)). Whether it is important that the mixing efficiency reduces as the bottom boundary is approached, or whether it is the stratification that goes to zero just above the boundary, by one means or another, or both, the turbulent buoyancy flux is zero at the sea floor, and this is the feature that causes the diapycnal upwelling in the BBL right near the boundary. This is an unavoidable consequence of the buoyancy budget, and applies no matter the nature of the many physical processes at play in the near-boundary region (Holmes and McDougall, 2020). The inevitability of the

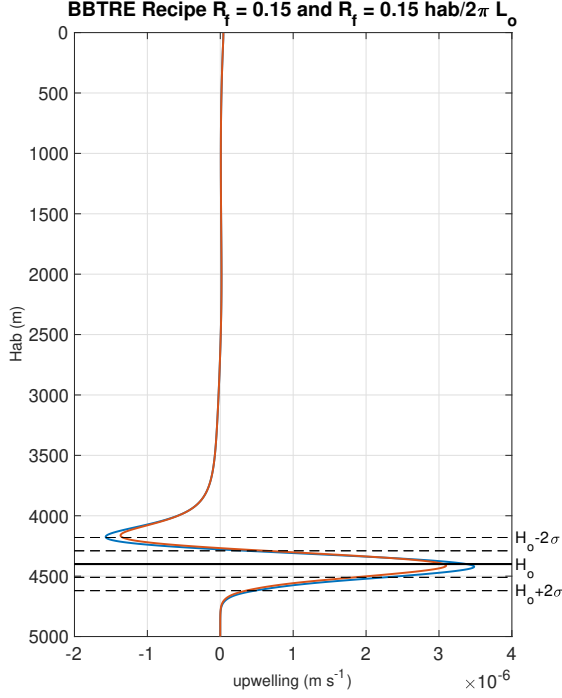**BBTRE Recipe $R_f = 0.15$ and $R_f = 0.15$ hab/2π L_o**

Figure 15: Diapycnal velocity profiles after invoking hypsometric arguments (33) and (34). The mean depth is assumed to be $H_o = 4400$ m and the root-mean-square topography $\sigma = 110$ m. Hypsometric effects extend several standard deviations about the mean. The blue trace appears in figure 6 of Polzin (2009). The red trace alters that estimate by reducing the observed dissipation with height above boundary to account for potential mixing metric limitations conjectured in Ferrari et al. (2016). The difference is minor and implies that the most important issue is the hypsometric constraints rather than the details of the near-bottom buoyancy flux profile.

upwards BBL diapycnal transport is captured in (21) and (22). These remarks are predicated on the idea that in the SML region, which on an vertical water column resides above the the top of the BBL, the complications caused by density reversals are largely absent.

Open Question #2b

Ferrari et al. (2016) argue for a generic near-boundary diminishment of mixing efficiency, presumably in conjunction with a suppression of length scales with decreasing distance from the boundary. Their argument is to assume that all three components of the density flux vector in (1d) scale as the vertical component. This may well be untrue: over sloping boundaries, turbulent density fluxes are fed by near-critical wave processes with horizontal fluxes are significantly larger than the vertical. We demonstrate this by writing the density flux vector in its Cartesian format:

$$\mathbf{F}_\rho = F_x \hat{i} + F_z \hat{k}$$

After rotating through the angle θ into slope normal and slope parallel coordinate system, the no-flux bottom boundary condition is

$$F_\perp|_{(z=h(x,y))} = F_z|_{(z=h(x,y))} \cos\theta - F_x|_{(z=h(x,y))} \sin\theta = 0$$
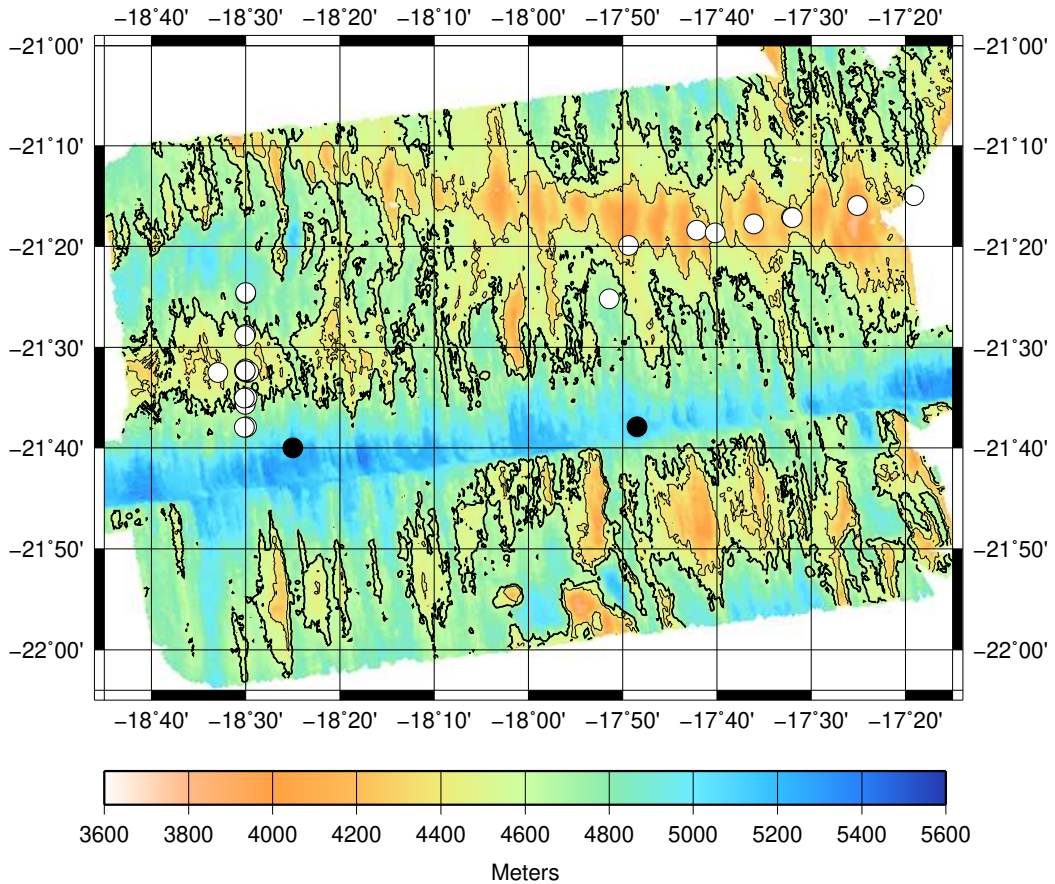
44

Figure 16: A 2-d representation of bathymetry appearing in figures 3 & 14. Two depth contours are drawn: a thick one representing 4400 m depth and a thin one at 4200 m depth. These contours are highly convoluted and the contour length depends upon the effective resolution of the underlying data. Higher and higher resolution will return longer and longer contour lengths. The figure domain is of similar size to the grid cell of a climate resolution GCM. Circles represent station positions for a subset of the profiles appearing in (Polzin et al., 1997; Ledwell et al., 2000) and figure 3. The blue shading represents the 'canyon' which is the subject of Thurnherr et al. (2005).

The Ferrari et al. argument is that

$$if \ \ F_x \ \cong \ F_z \ ,$$
(35a)

then, in a small angle approximation,

$$F_\perp|_{(z=h(x,y))} \ \cong \ F_z|_{(z=h(x,y))} = 0 \ .$$
(35b)

The observational constraint that turbulent dissipation ϵ increases with decreasing height above boundary and the assumption (35a) thus lead Ferrari et al. (2016) to assume that the mixing metric Γ decreases more quickly than ϵ increases such that F_z attains a relative minimum off the bottom, with the consequence of downwelling above the relative minimum and upwelling below via (9).

The relation (35a) is buttressed by an intuitive notion of a length scale suppression grounded in the paradigm of steady flows, stable stratification and a wealth of atmospheric boundary layer lore obtained over flat bottoms. The issue of mixing above a sloping boundary could be qualitatively different. Here, turbulence is linked to internal wave processes in which the issue of a critical slope figures prominently. *If*, for example, we choose to scale the horizontal fluxes using basic internal wave kinematics (32),

$$\frac{F_x}{F_z} \equiv \frac{\overline{u'\theta'}}{\overline{w'\theta'}} \ \sim \ \frac{u'_{rms}\theta'_{rms}}{w'_{rms}\theta'_{rms}} \cong \frac{N\sqrt{\omega(\alpha)^2 + f^2}}{\omega(\alpha)\sqrt{\omega(\alpha)^2 - f^2}}$$
(36)

the bottom boundary condition becomes

$$F_\perp|_{(z=h(x,y))} \ \cong \ F_z|_{(z=h(x,y))} \left[\cos\theta - \frac{N\sqrt{\omega(\alpha)^2 + f^2}}{\omega(\alpha)\sqrt{\omega(\alpha)^2 - f^2}} \ \sin(\theta) \right] \cong 0$$

such that *no* constraint upon $F_z|_{(z=h(x,y))}$ is implied due to the subtractive cancellation of the geometric terms in the square brackets. The scaling (36) is motivated by internal wave band temperature fluxes reported by van Haren and collaborators (van Haren et al., 1994; Gemmrich and van Haren, 2002).

With such a proposed scaling it also should be appreciated that there are phenomenological differences between a critical frequency process and steady shear flow. A key feature of critical frequency processes is not only that of reversals in cross-slope flow, it is the episodic occurrence of statically unstable conditions related to the differential advection of density associated with a near-critical nature of the internal wave field forming large scale overturning events (Sarkar and Scotti, 2017). Similar issues arise in the downwelling Ekman layer in which the buoyancy flux is accomplished via the agency of the critical frequency wave rather than in conjunction with the bottom stress.

Our orthogonality of opinion is captured by reactions to figure 2. When you see the weak stratification near the boundary, do you think about the mixing of mixed water and decreasing buoyancy flux as the bottom is approached, or do you see the potential for a convective process and imagine a highly efficient mixing process with large near-bottom buoyancy fluxes captured in figure 12? The former opinion is aided and abetted by models that simply assume a diffusivity profile and solve for the buoyancy and velocity fields rather than engaging with turbulence modeling.

Near boundary microstructure estimates that might resolve this disparate point of view are difficult to come by, especially within an abyssal setting. Within the context of a highly stratified estuary, Holleman et al. (2016) use inertial subrange estimates of ϵ and χ to document a 'boundary influenced' regime of decreased Γ over a height scale $h(x,y) < 2\pi L_o$. If we translate this to the Brazil Basin, near-bottom estimates of $\epsilon = 1 \times 10^{-8}$ W/kg and $N^2 = 1 \times 10^{-3}$ s^{-2} returns $2\pi L_o = 20$ m. There is little observational constraint: regions closer that 20 m to the bottom were unsampled by the free-fall instrumentation. While an observational constraint is lacking, one can certainly pose the question of whether the root of the Ferrari et al. (2016) conjecture concerning the structure of Γ is the issue of GCM behavior when the GCM lacks an adequate representation of rough topography. To address this, the mixing metric Γ in (34) was changed from a constant 0.2 to decrease linearly to zero over the bottom-most 20 meters and the hysometric arguments (33) and (34) repeated. The end result appears along side the original upwelling assessment in figure 15: an $O(10\%)$ change is noted in the diapycnal upwelling profile. Hypsometry dominates. Holmes and McDougall (2020) did consider the fact that while the buoyancy flux through the sloping sea floor is zero, the turbulent buoyancy flux parallel to the boundary is non-zero, as discussed in this section. However, they found that the lateral convergence of these buoyancy fluxes parallel to the sloping sea floor was unlikely to be large enough to reverse the upward flow in the BBL even at individual locations, let alone over a significant area of the sea floor.

Open Question #3: Communication with the Interior

One of the issues posed with figure 2 is how one avoids the state in which water near the boundary becomes weakly stratified. The proposal in figure 15 might be applicable for the Mid-Atlantic Ridge, but is likely not a generic solution to that problem. In Callies (2018) we find baroclinic instability to be an elegant (simple) way of restratifying the interor. The closure that is offered suggests a rather uniform diffusive process.

This contrasts with the apparent time history of a tracer release in the Gulf of Mexico reported in Ledwell et al. (2016), in which near boundary tracer was swept off-slope in single, semi-deterministic event. One can also create a list of possible ventillation processes: internal hydraulic transitions, internal bores and flow separation represent efficient ways to expel mass from the boundary and accomplish a wholesale reset of near-boundary stratification that compete with restratification via baroclinic instability.

Open Question #4: Whither Entrainment/Detrainment Arguments in Abyssal Plumes?

It has traditionally been assumed that sinking plumes of Bottom Water continually entrain water into them, thus increasing their volume transport as they sink towards the abyss. This however leads to contradictions as outlined in section 3. Do we overcome these issues by appealing to the modern realization that sinking plumes can detrain as well as entrain, or do we need to consider multiple sources of Bottom Water as another way out of these contradictions? We note that both the Brazil Basin and the Orkney Passage measurement programs have been made in these descending plumes of dense Bottom Water, so these locations may not be typical of more general rough sea floor boundary locations.

Acknowledgments

General

Author Contributions

Funding

Conflicts of Interest

The authors declare that there is no conflict of interest regarding the publication of this article.

Data Availability

No data were created as part of this review.

References

Alford, M.H., Girton, J.B., Voet, G., Carter, G.S., Mickett, J.B., Klymak, J.M., 2013. Turbulent mixing and hydraulic control of abyssal water in the samoan passage. Geophysical research letters 40, 4668–4674.

Allen, J., Newberger, P., 1998. On symmetric instabilities in oceanic bottom boundary layers. Journal of physical oceanography 28, 1131–1151.

Armi, L., 1978. Some evidence for boundary mixing in the deep ocean. Journal of Geophysical Research: Oceans 83, 1971–1979.

Armi, L., 1979a. Effects of variations in eddy diffusivity on property distributions in the oceans. Journal of Marine Research 37, 515–530.

Armi, L., 1979b. Reply to comments by C. Garrett. Journal of Geophysical Research: Oceans 84, 5097–5098.

Armi, L., Millard Jr, R.C., 1976. The bottom boundary layer of the deep ocean. Journal of Geophysical Research 81, 4983–4990.

Baines, P., 1973. The generation of internal tides by flat-bump topography, in: Deep Sea Research and Oceanographic Abstracts, Elsevier. pp. 179–205.

Baines, P.G., 1997. Topographic effects in stratified flows. Cambridge university press.

Baines, P.G., 2001. Mixing in flows down gentle slopes into stratified environments. Journal of Fluid Mechanics 443, 237.

Baines, P.G., 2005. Mixing regimes for the flow of dense fluid down slopes into stratified environments. Journal of Fluid mechanics 538, 245.

Bracco, A., Paris, C.B., Esbaugh, A.J., Frasier, K., Joye, S., Liu, G., Polzin, K., Vaz, A.C., 2020. Transport, fate and impacts of the deep plume of petroleum hydrocarbons formed during the macondo blowout. Frontiers in Marine Science 7, 764.

Brearley, J.A., Sheen, K.L., Naveira Garabato, A.C., Smeed, D.A., Waterman, S., 2013. Eddy-induced modulation of turbulent dissipation over rough topography in the southern ocean. Journal of physical oceanography 43, 2288–2308.

Bretherton, F.P., 1969. Momentum transport by gravity waves. Quarterly Journal of the Royal Meteorological Society 95, 213–243.

Brink, K.H., Lentz, S.J., 2010. Buoyancy arrest and bottom ekman transport. part i: Steady flow. Journal of Physical Oceanography 40, 621–635.

Brown, N., 1974. A precision ctd microprofiler, in: Ocean'74-IEEE International Conference on Engineering in the Ocean Environment, IEEE. pp. 270–278.

Bryan, K., Lewis, L., 1979. A water mass model of the world ocean. Journal of Geophysical Research: Oceans 84, 2503–2517.

Callies, J., 2018. Restratification of abyssal mixing layers by submesoscale baroclinic eddies. Journal of Physical Oceanography 48, 1995–2010.

Callies, J., Ferrari, R., 2018. Dynamics of an abyssal circulation driven by bottom-intensified mixing on slopes. Journal of Physical Oceanography 48, 1257–1282.

Chalamalla, V.K., Gayen, B., Scotti, A., Sarkar, S., 2013. Turbulence during the reflection of internal gravity waves at critical and near-critical slopes. Journal of Fluid Mechanics 729, 47.

Chalamalla, V.K., Sarkar, S., 2015. Mixing, dissipation rate, and their overturn-based estimates in a near-bottom turbulent flow driven by internal tides. Journal of Physical Oceanography 45, 1969–1987.

Clément, L., Frajka-Williams, E., Sheen, K., Brearley, J., Garabato, A.N., 2016. Generation of internal waves by eddies impinging on the western boundary of the north atlantic. Journal of Physical Oceanography 46, 1067–1079.

Clément, L., Thurnherr, A.M., 2018. Abyssal upwelling in mid-ocean ridge fracture zones. Geophysical Research Letters 45, 2424–2432.

Cusack, J.M., Brearley, J.A., Naveira Garabato, A.C., Smeed, D.A., Polzin, K.L., Velzeboer, N., Shakespeare, C.J., 2020. Observed eddy–internal wave interactions in the southern ocean. Journal of Physical Oceanography 50, 3043–3062.

Cusack, J.M., Voet, G., Alford, M.H., Girton, J.B., Carter, G.S., Pratt, L.J., Pearson-Potts, K.A., Tan, S., 2019. Persistent turbulence in the samoan passage. Journal of Physical Oceanography 49, 3179–3197.

Cushman-Roisin, B., Beckers, J.M., 2011. Introduction to geophysical fluid dynamics: physical and numerical aspects. Academic press.

Drake, H.F., Ferrari, R., Callies, J., 2020. Abyssal circulation driven by near-boundary mixing: water mass transformations and interior stratification. Journal of Physical Oceanography 50, 2203–2226.

Epifanio, C.C., Durran, D.R., 2001. Three-dimensional effects in high-drag-state flows over long ridges. Journal of the Atmospheric Sciences 58, 1051–1065.

Eriksen, C.C., 1982. Observations of internal wave reflection off sloping bottoms. Journal of Geophysical Research: Oceans 87, 525–538.

Eriksen, C.C., 1985. Implications of ocean bottom reflection for internal wave spectra and mixing. Journal of Physical Oceanography 15, 1145–1156.

Eriksen, C.C., 1998. Internal wave reflection and mixing at Fieberling Guyot. Journal of Geophysical Research 103, 2977–2994.

Evans, D.G., Frajka-Williams, E., Garabato, A.N., Polzin, K., 2020. Mesoscale eddy dissipation by a 'zoo' of submesoscale processes at a western boundary. Journal of Geophysical Research: Oceans 125.

Ferrari, R., Mashayek, A., McDougall, T.J., Nikurashin, M., Campin, J.M., 2016. Turning ocean mixing upside down. Journal of Physical Oceanography 46, 2239–2261.

Ferrari, R., Polzin, K.L., 2005. Finescale structure of the t–s relation in the eastern north atlantic. Journal of Physical Oceanography 35, 1437–1454.

Ferron, B., Mercier, H., Speer, K., Gargett, A., Polzin, K., 1998. Mixing in the Romanche Fracture Zone. Journal of Physical Oceanography 28, 1929–1945.

Gardiner, C.W., et al., 1985. Handbook of stochastic methods. volume 3. springer Berlin.

Garrett, C., 1979. Comment on 'some evidence for boundary mixing in the deep ocean' by Laurence Armi. Journal of Geophysical Research: Oceans 84, 5095–5095.

Garrett, C., 1984. Turning points in universal speculation on internal waves. A celebration in Geophysics and Oceanography 84, 38–46.

Garrett, C., 1990. The role of secondary circulation in boundary mixing. Journal of Geophysical Research: Oceans 95, 3181–3188.

Garrett, C., 1991. Marginal mixing theories. Atmosphere-Ocean 29, 313–339.

Garrett, C., 2001. An isopycnal view of near-boundary mixing and associated flows. Journal of physical oceanography 31, 138–142.

Garrett, C., Gilbert, D., 1988. Estimates of vertical mixing by internal waves reflected off a sloping bottom, in: Elsevier oceanography series. Elsevier. volume 46, pp. 405–423.

Garrett, C., MacCready, P., Rhines, P., 1993. Boundary mixing and arrested ekman layers: Rotating stratified flow near a sloping boundary. Annual Review of Fluid Mechanics 25, 291–323.

Garrett, C., Munk, W., 1972a. Oceanic mixing by breaking internal waves, in: Deep sea research and oceanographic abstracts, Elsevier. pp. 823–832.

Garrett, C., Munk, W., 1972b. Space-time scales of internal waves. Geophysical & Astrophysical Fluid Dynamics 3, 225–264.

Gayen, B., Sarkar, S., 2010. Turbulence during the generation of internal tide on a critical slope. Physical review letters 104, 218502.

Gemmrich, J.R., van Haren, H., 2002. Internal wave band eddy fluxes above a continental slope. Journal of Marine Research 60, 227–253. doi:doi:10.1357/00222400260497471.

Gent, P.R., Willebrand, J., McDougall, T.J., McWilliams, J.C., 1995. Parameterizing eddy-induced tracer transports in ocean circulation models. Journal of Physical Oceanography 25, 463–474.

Goff, J.A., Jordan, T.H., 1988. Stochastic modelling of seafloor morphology: Inversion of Sea Beam data for second-order statistics. Journal of Geophysical Research 93, 13,589–13,608.

Greatbatch, R.J., Lamb, K.G., 1990. On parameterizing vertical mixing of momentum in non-eddy resolving ocean models. Journal of Physical Oceanography 20, 1634–1637.

Gregg, M., Cox, C., 1971. Measurements of the oceanic microstructure of temperature and electrical conductivity, in: Deep Sea Research and Oceanographic Abstracts, Elsevier. pp. 925–934.

Gregg, M., D'Asaro, E., Riley, J., Kunze, E., 2018. Mixing efficiency in the ocean. Annual Review of Marine Science 10, 443–473. doi:10.1146/annurev-marine-121916-063643.

Group, M., et al., 1978. The mid-ocean dynamics experiment. Deep Sea Research 25, 859–910.

van Haren, H., Oakey, N., Garrett, C., 1994. Measurements of internal wave band eddy fluxes above a sloping bottom. Journal of Marine Research 52, 909–946.

Hasselmann, K., 1962. On the non-linear energy transfer in a gravity-wave spectrum part 1. general theory. Journal of Fluid Mechanics 12, 481–500.

Hogg, C.A., Dalziel, S.B., Huppert, H.E., Imberger, J., 2017. Inclined gravity currents filling basins: the impact of peeling detrainment on transport and vertical structure. Journal of Fluid Mechanics 820, 400.

Hogg, N., Biscaye, P., Gardner, W., Schmitz Jr, W.J., 1982. On the transport and modification of antarctic bottom water in the vema channel. J. Mar. Res 40, l–263.

Hogg, N.G., 1983. Hydraulie control and flow separation in a multi-layered fluid with applications to the vema channel. Journal of Physical Oceanography 13, 695–708.

Holleman, R.C., Geyer, W.R., Ralston, D.K., 2016. Stratified turbulence and mixing efficiency in a salt wedge estuary. Journal of Physical Oceanography 46, 1769–1783. doi:10.1175/JPO-D-15-0193.1.

Holmes, R., de Lavergne, C., McDougall, T.J., 2019. Tracer transport within abyssal mixing layers. Journal of Physical Oceanography 49, 2669–2695.

Holmes, R., McDougall, T.J., 2020. Diapycnal transport near a sloping bottom boundary. Journal of Physical Oceanography 50, 3252–3266.

Holmes, R.M., de Lavergne, C., McDougall, T.J., 2018. Ridges, seamounts, troughs, and bowls: Topographic control of the dianeutral circulation in the abyssal ocean. Journal of Physical Oceanography 48, 861–882.

Ijichi, T., St. Laurent, L., Polzin, K.L., Toole, J.M., 2020. How variable is mixing efficiency in the abyss? Geophysical Research Letters 47, e2019GL086813.

IOC, S., 2010. Iapso, 2010: The international thermodynamic equation of seawater—2010: Calculation and use of thermodynamic properties. Intergovernmental Oceanographic Commission, Manuals and Guides 56, 220.

Iudicone, D., Madec, G., McDougall, T.J., 2008. Water-mass transformations in a neutral density framework and the key role of light penetration. Journal of Physical Oceanography 38, 1357–1376.

Jayne, S.R., 2009. The impact of abyssal mixing parameterizations in an ocean general circulation model. Journal of Physical Oceanography 39, 1756–1775.

Kaimal, J., Wyngaard, J., Izumi, Y., Cote, O., 1972. Spectral characteristics of surface-layer turbulence. Quarterly Journal of the Royal Meteorological Society 98, 563–589.

Kaiser, B., Pratt, L.J., 2020. The transition to turbulence within internal tide boundary layers in the abyssal ocean., in: Ocean Sciences Meeting 2020, AGU.

Kamenkovich, V., Monin, A., Voorhis, A., 1986. The Polymode Atlas. Woods Hole oceanographic institution.

Klocker, A., McDougall, T.J., 2010. Influence of the nonlinear equation of state on global estimates of dianeutral advection and diffusion. Journal of Physical Oceanography 40, 1690–1709.

Klymak, J.M., Legg, S., Pinkel, R., 2010. A simple parameterization of turbulent mixing near supercritical topography. Journal of Physical Oceanography 40, 2059–2074.

Kolås, E., Fer, I., 2018. Hydrography, transport and mixing of the west spitsbergen current: the svalbard branch in summer 2015. Ocean Science 14, 1603–1618.

Kunze, E., Lien, R.C., 2019. Energy sinks for lee waves in shear flow. Journal of Physical Oceanography 49, 2851–2865.

Kunze, E., MacKay, C., McPhee-Shaw, E.E., Morrice, K., Girton, J.B., Terker, S.R., 2012. Turbulent mixing and exchange with interior waters on sloping boundaries. Journal of physical oceanography 42, 910–927.

de Lavergne, C., Madec, G., Le Sommer, J., Nurser, A.G., Naveira Garabato, A.C., 2016a. On the consumption of antarctic bottom water in the abyssal ocean. Journal of Physical Oceanography 46, 635–661.

de Lavergne, C., Madec, G., Le Sommer, J., Nurser, A.J.G., Naveira Garabato, A.C., 2016b. The impact of a variable mixing efficiency on the abyssal overturning. Journal of Physical Oceanography 46, 663–681. doi:10.1175/JPO-D-14-0259.1.

de Lavergne, C., Madec, G., Roquet, F., Holmes, R., McDougall, T.J., 2017. Abyssal ocean overturning shaped by seafloor distribution. Nature 551, 181–186.

Ledwell, J., Montgomery, E., Polzin, K., Laurent, L.S., Schmitt, R., Toole, J., 2000. Evidence for enhanced mixing over rough topography in the abyssal ocean. Nature 403, 179–182.

Ledwell, J.R., He, R., Xue, Z., DiMarco, S.F., Spencer, L.J., Chapman, P., 2016. Dispersion of a tracer in the deep gulf of mexico. Journal of Geophysical Research: Oceans 121, 1110–1132.

Ledwell, J.R., Watson, A.J., Law, C.S., 1998. Mixing of a tracer in the pycnocline. Journal of Geophysical Research: Oceans 103, 21499–21529.

Lentz, S.J., Trowbridge, J.H., 1991. The bottom boundary layer over the northern california shelf. Journal of Physical Oceanography 21, 1186–1201.

Lumpkin, R., Speer, K., 2007. Global ocean meridional overturning. Journal of Physical Oceanography 37, 2550–2562.

MacCready, P., Rhines, P.B., 1991. Buoyant inhibition of ekman transport on a slope and its effect on stratified spin-up. Journal of Fluid Mechanics 223, 631–661.

MacCready, P., Rhines, P.B., 1993. Slippery bottom boundary layers on a slope. Journal of Physical Oceanography 23, 5–22.

MacKinnon, J.A., Johnston, T.M.S., Pinkel, R., 2008. Strong transport and mixing of deep water through the Southwest Indian Ridge. Nature Geoscience 1. doi:10.1037/ngeo340.

Mandelbrot, B.B., Mandelbrot, B.B., 1982. The fractal geometry of nature. volume 1. WH freeman New York.

Marshall, J., Jamous, D., Nilsson, J., 1999. Reconciling thermodynamic and dynamic methods of computation of water-mass transformation rates. Deep Sea Research Part I: Oceanographic Research Papers 46, 545–572.

Mashayek, A., Caulfield, C.P., Peltier, W.R., 2017. Role of overturns in optimal mixing in stratified mixing layers. Journal of Fluid Mechanics 826, 522?552. doi:10.1017/jfm.2017.374.

Mauritzen, C., Polzin, K.L., McCartney, M.S., Millard, R.C., West-Mack, D.E., 2002. Evidence in hydrography and density finestructure for enhanced vertical mixing over the Mid-Atlantic Ridge in the western Atlantic. Journal of Geophysical Research 107. doi:10.1029/2001JC 001114.

McComas, C.H., Bretherton, F.P., 1977. Resonant interaction of oceanic internal waves. Journal of Geophysical Research 82, 1397–1412.

McDougall, T.J., 1984. The relative roles of diapycnal and isopycnal mixing on subsurface water mass conversion. Journal of Physical Oceanography 14, 1577–1589.

McDougall, T.J., 1989. Dianeutral advection, in: Parameterization of Small-Scale Processes: Proc.'Aha Huliko 'a Hawaiian Winter Workshop, pp. 289–315.

McDougall, T.J., Ferrari, R., 2017. Abyssal upwelling and downwelling driven by near-boundary mixing. Journal of Physical Oceanography 47, 261–283. doi:10.1175/JPO-D-16-0082.1.

McDougall, T.J., McIntosh, P.C., 2001. The temporal-residual-mean velocity. part ii: Isopycnal interpretation and the tracer and momentum equations. Journal of Physical Oceanography 31, 1222–1246.

Melet, A., Hallberg, R., Legg, S., Polzin, K., 2013. Sensitivity of the ocean state to the vertical distribution of internal-tide-driven mixing. Journal of Physical Oceanography 43, 602–615.

Mellor, G.L., Yamada, T., 1974. A hierarchy of turbulence closure models for planetary boundary layers. Journal of the atmospheric sciences 31, 1791–1806.

Mercier, H., Morin, P., 1997. Hydrography of the romanche and chain fracture zones. Journal of Geophysical Research: Oceans 102, 10373–10389.

Mercier, H., Speer, K.G., 1998. Transport of bottom water in the romanche fracture zone and the chain fracture zone. Journal of Physical Oceanography 28, 779–790.

Morris, M.Y., Hall, M.M., St. Laurent, L.C., Hogg, N.G., 2001. Abyssal mixing in the brazil basin. Journal of physical oceanography 31, 3331–3348.

Moum, J., Perlin, A., Klymak, J., Levine, M., Boyd, T., Kosro, P., 2004. Convectively driven mixing in the bottom boundary layer. Journal of physical oceanography 34, 2189–2202.

Munk, W., Wunsch, C., 1998. Abyssal recipes ii: Energetics of tidal and wind mixing. Deep-sea research. Part I, Oceanographic research papers 45, 1977–2010.

Munk, W.H., 1966. Abyssal recipes, in: Deep Sea Research and Oceanographic Abstracts, Citeseer. pp. 707–730.

Nash, J.D., Moum, J.N., 2001. Internal hydraulic flows on the continental shelf: High drag states over a small bank. Journal of Geophysical Research: Oceans 106, 4593–4611. doi:10.1029/1999JC000183.

Nasmyth, P.W., 1970. Oceanic turbulence. Ph.D. thesis. University of British Columbia.

Naveira Garabato, A.C., Frajka-Williams, E.E., Spingys, C.P., Legg, S., Polzin, K.L., Forryan, A., Abrahamsen, E.P., Buckingham, C.E., Griffies, S.M., McPhail, S.D., Nicholls, K.W., Thomas, L.N., Meredith, M.P., 2019. Rapid mixing and exchange of deep-ocean waters in an abyssal boundary current. Proceedings of the National Academy of Sciences 116, 13233–13238. doi:10.1073/pnas.1904087116.

Naveira Garabato, A.C., Polzin, K.L., King, B.A., Heywood, K.J., Visbeck, M., 2004. Widespread intense turbulent mixing in the Southern Ocean. Science 303, 210–213.

Nikurashin, M., Ferrari, R., 2010. Radiation and dissipation of internal waves generated by geostrophic motions impinging on small-scale topography: Theory. Journal of Physical Oceanography 40, 1055–1074.

Nikurashin, M., Ferrari, R., 2011. Global energy conversion rate from geostrophic flows into internal lee waves in the deep ocean. Geophysical Research Letters 38.

Nikurashin, M., Ferrari, R., 2013. Overturning circulation driven by breaking internal waves in the deep ocean. Geophysical Research Letters 40, 3133–3137.

Nikurashin, M., Ferrari, R., Grisouard, N., Polzin, K., 2014. The impact of finite-amplitude bottom topography on internal wave generation in the southern ocean. Journal of Physical Oceanography 44, 2938–2950.

Olbers, D.J., 1976. Nonlinear energy transfer and the energy balance of the internal wave field in the deep ocean. Journal of Fluid mechanics 74, 375–399.

Osborn, T., 1980. Estimates of the local rate of vertical diffusion from dissipation measurements. Journal of physical oceanography 10, 83–89.

Osborn, T., Siddon, T., 1973. Oceanic shear measurements using the airfoil probe .

Osborn, T.R., Cox, C.S., 1972. Oceanic fine structure. Geophysical Fluid Dynamics 3, 321–345.

Perlin, A., Moum, J.N., Klymak, J., Levine, M.D., Boyd, T., Kosro, P.M., 2005. A modified law-of-the-wall applied to oceanic bottom boundary layers. Journal of Geophysical Research: Oceans 110.

Phillips, O., 1960. On the dynamics of unsteady gravity waves of finite amplitude part 1. the elementary interactions. Journal of Fluid Mechanics 9, 193–217.

Phillips, O., 1970. On flows induced by diffusion in a stably stratified fluid, in: Deep Sea Research and Oceanographic Abstracts, Elsevier. pp. 435–443.

Phillips, O., Shyu, J.H., Salmun, H., 1986. An experiment on boundary mixing: mean circulation and transport rates. Journal of fluid mechanics 173, 473–499.

Polzin, K., Toole, J., Ledwell, J., Schmitt, R., 1997. Spatial variability of turbulent mixing in the abyssal ocean. Science 276, 93–96.

Polzin, K.L., 2004a. A heuristic description of internal wave dynamics. Journal of Physical Oceanography 34, 214–230.

Polzin, K.L., 2004b. Idealized solutions for the energy balance of the finescale internal wavefield. Journal of Physical Oceanography 34, 231–246.

Polzin, K.L., 2009. An abyssal recipe. Ocean Modelling 30, 298–309.

Polzin, K.L., Lvov, Y.V., 2017. An oceanic ultra-violet catastrophe, wave-particle duality and a strongly nonlinear concept for geophysical turbulence. Fluids 2, 36.

Polzin, K.L., Speer, K., Toole, J.M., Schmitt, R.W., 1996. Mixing in the Romanche Fracture Zone. Nature 380, 54–57.

Pomphrey, N., Meiss, J.D., Watson, K.M., 1980. Description of nonlinear internal wave interactions using langevin methods. Journal of Geophysical Research: Oceans 85, 1085–1094.

Rhines, P.B., 1993. Oceanic general circulation: Wave and advection dynamics, in: Modelling Oceanic Climate Interactions. Springer, pp. 67–149.

Ruan, X., Thompson, A.F., Taylor, J.R., 2019. The evolution and arrest of a turbulent stratified oceanic bottom boundary layer over a slope: Downslope regime. Journal of Physical Oceanography 49, 469–487.

Sanford, T.B., 1975. Observations of the vertical structure of internal waves. Journal of Geophysical Research 80, 3861–3871.

Sarkar, S., Scotti, A., 2017. From topographic internal gravity waves to turbulence. Annual Review of Fluid Mechanics 49, 195–220.

Schiff, L., 1966. Lateral boundary mixing in a simple model of ocean convection, in: Deep Sea Research and Oceanographic Abstracts, Elsevier. pp. 621–626.

Scott, R., Goff, J., Naveira Garabato, A., Nurser, A., 2011. Global rate and spectral characteristics of internal gravity wave generation by geostrophic flow over topography. Journal of Geophysical Research: Oceans 116.

Shaw, W.J., Trowbridge, J.H., Williams III, A.J., 2001. Budgets of turbulent kinetic energy and scalar variance in the continental shelf bottom boundary layer. Journal of Geophysical Research: Oceans 106, 9551–9564. doi:10.1029/2000JC000240.

Shih, L.H., Koseff, J.R., Ivey, G.N., Ferziger, J.H., 2005. Parameterization of turbulent fluxes and scales using homogeneous sheared stably stratified turbulence simulations. Journal of Fluid Mechanics 525, 193?214. doi:10.1017/S0022112004002587.

Slinn, D.N., Riley, J., 1998. Turbulent dynamics of a critically reflecting internal gravity wave. Theoretical and computational fluid dynamics 11, 281–303.

Smyth, W., Moum, J., Caldwell, D., 2001. The efficiency of mixing in turbulent patches: Inferences from direct simulations and microstructure observations. Journal of Physical Oceanography 31, 1969–1992.

Spingys, C., Naveira Garabato, A., Legg, S., Polzin, K., Abrahamsen, P., Buckingham, C., Forryan, A., Frajka-Williams, E., 2001-in press. Mixing and transformation in a deep western boundary current: A case study. Journal of Physical Oceanography .

Sreenivasan, K.R., 1995. On the universality of the kolmogorov constant. Physics of Fluids 7, 2778–2784. doi:10.1063/1.868656.

Sreenivasan, K.R., 1996. The passive scalar spectrum and the obukhov–corrsin constant. Physics of Fluids 8, 189–196. doi:10.1063/1.868826.

St Laurent, L.C., Thurnherr, A.M., 2007. Intense mixing of lower thermocline water on the crest of the mid-atlantic ridge. Nature 448, 680–683.

St. Laurent, L.C., Toole, J.M., Schmitt, R.W., 2001. Buoyancy forcing by turbulence above rough topography in the abyssal brazil basin. Journal of Physical Oceanography 31, 3476–3495.

Stommel, H., Arons, A., 1959. On the abyssal circulation of the world ocean—i. stationary planetary flow patterns on a sphere. Deep Sea Research (1953) 6, 140–154.

Stull, R.B., 2012. An introduction to boundary layer meteorology. volume 13. Springer Science & Business Media.

Taylor, J.R., Sarkar, S., 2008. Stratification effects in a bottom ekman layer. Journal of Physical oceanography 38, 2535–2555.

Tennekes, H., Lumley, J., 1972. A first course in turbulence.

Thorpe, S., Malarkey, J., Voet, G., Alford, M., Girton, J., Carter, G., 2018. Application of a model of internal hydraulic jumps. Journal of Fluid Mechanics 834, 125–148.

Thorpe, S.A., 1977. Turbulence and mixing in a scottish loch. Philosophical Transactions of the Royal Society of London. Series A, Mathematical and Physical Sciences 286, 125–181.

Thorpe, S.A., 1987. Current and temperature variability on the continental slope. Philosophical Transactions of the Royal Society of London. Series A, Mathematical and Physical Sciences 323, 471–517.

Thorpe, S.A., 1992. The generation of internal waves by flow over the rough topography of a continental slope. Proceedings of the Royal Society of London. Series A: Mathematical and Physical Sciences 439, 115–130.

Thurnherr, A., 2006. Diapycnal mixing associated with an overflow in a deep submarine canyon. Deep Sea Research Part II: Topical Studies in Oceanography 53, 194–206.

Thurnherr, A., St. Laurent, L., Speer, K., Toole, J., Ledwell, J., 2005. Mixing associated with sills in a canyon on the midocean ridge flank. Journal of physical oceanography 35, 1370–1381.

Thurnherr, A.M., Clément, L., St. Laurent, L., Ferrari, R., Ijichi, T., 2020. Transformation and upwelling of bottom water in fracture zone valleys. Journal of Physical Oceanography 50, 715–726.

Tippenhauer, S., Dengler, M., Fischer, T., Kanzow, T., 2015. Turbulence and finestructure in a deep ocean channel with sill overflow on the mid-atlantic ridge. Deep Sea Research Part I: Oceanographic Research Papers 99, 10–22.

Toole, J.M., Schmitt, R.W., Polzin, K.L., Kunze, E., 1997. Near-boundary mixing above the flanks of a midlatitude seamount. Journal of Geophysical Research: Oceans 102, 947–959.

Trowbridge, J., Lentz, S., 1991. Asymmetric behavior of an oceanic boundary layer above a sloping bottom. Journal of Physical Oceanography 21, 1171–1185.

Trowbridge, J.H., Lentz, S.J., 2018. The bottom boundary layer. Annual Review of Marine Science 10, 397–420.

Umlauf, L., Smyth, W.D., Moum, J.N., 2015. Energetics of bottom ekman layers during buoyancy arrest. Journal of Physical Oceanography 45, 3099–3117.

Voet, G., Girton, J.B., Alford, M.H., Carter, G.S., Klymak, J.M., Mickett, J.B., 2015. Pathways, volume transport, and mixing of abyssal water in the samoan passage. Journal of Physical Oceanography 45, 562–588.

Walin, G., 1982. On the relation between sea-surface heat flow and thermal circulation in the ocean. Tellus 34, 187–195.

Waterhouse, A.F., MacKinnon, J.A., Nash, J.D., Alford, M.H., Kunze, E., Simmons, H.L., Polzin, K.L., St. Laurent, L.C., Sun, O.M., Pinkel, R., et al., 2014. Global patterns of diapycnal mixing from measurements of the turbulent dissipation rate. Journal of Physical Oceanography 44, 1854–1872.

Weatherly, G.L., Martin, P.J., 1978. On the structure and dynamics of the oceanic bottom boundary layer. Journal of Physical Oceanography 8, 557–570.

Whitehead Jr, J., Worthington, L., 1982. The flux and mixing rates of antarctic bottom water within the north atlantic. Journal of Geophysical Research: Oceans 87, 7903–7924.

Wunsch, C., 1970. On oceanic boundary mixing, in: Deep Sea Research and Oceanographic Abstracts, Elsevier. pp. 293–301.

Wyrtki, K., 1961. The thermohaline circulation in relation to the general circulation in the oceans. Deep Sea Research (1953) 8, 39–64.

Wyrtki, K., 1962. The oxygen minima in relation to ocean circulation, in: Deep Sea Research and Oceanographic Abstracts, Elsevier. pp. 11–23.